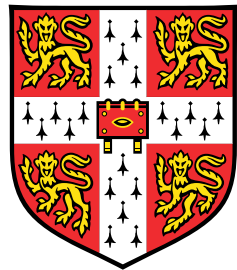


# Numerical Study of the Interaction between Fluid and Multiple Cylinders



**Zhonglu Lin**

Department of Engineering  
University of Cambridge

This dissertation is submitted as  
*First Year Report*

Jesus College

April 2018



Supervisor: Dr. Dongfang Liang  
Advisor: Dr. Fehmi Cirak



## **Acknowledgements**

I would like to thank my supervisor, Dr. Dongfang Liang, for his academic support on my research. My application could not be successful without his support.

I would like to express my gratitude to Prof. Ming Zhao from Western Sydney University for providing the code, sharing the computational resources, advice on mesh generation issues, and offering the validation data.

I am also indebted to Xuanyu Zhao, without whose advice and encouragement my application could not be successful.

I would also like to thank my desk mate Vitaly Levdik, who has improved my presentation skills and logical thinking.

I would also like to thank Shidi Yan, Xiao Xiao, Xuanyu and Zhengtao Shen for proof-reading this report.

Thanks are also due to my parents. I thank them dearly for their financial support and encouragement for my pursuit of a Ph.D. degree.

I appreciate the help from my office mates: John Wang, Yishu Wang, Ruodan Lu. They have taught me knowledge in engineering and beyond.

I would like to thank Lei Shi, who offered me a great deal of emotional support.

At last, a thank you to Chunwen Xiao, who has taught me a lot and has motivated me to pursue higher aims both in my research and in my life.



## Abstract

The interaction between two adjacent cylinders immersed in fluid is studied numerically by solving the two-dimensional Navier-Stokes (NS) equations using a finite element method (FEM). The two rigid cylinders are immersed in otherwise stationary fluid. One cylinder (C1) undergoes forced vibration that disturbs the fluid, whereas another cylinder (C2), which has one-degree-of-freedom (1DOF), vibrates correspondingly under the action of the imbalanced hydrodynamic force. All the simulations carried out in this study have a constant Reynolds number of 100 and a constant mass ratio of 2.5. Simulations are conducted with a series gap ratios,  $G$ , ranging from 0.025 to 3 times of the cylinder diameter, with various forced vibration amplitude  $A_1$  and frequency  $f_1$  of C1. We find that C2's amplitude ( $A_2$ ) reaches maximum when C1's vibration frequency ( $f_1$ ) is approximately 80% of C2's structural natural frequency ( $f_n$ ). The increase of C1's amplitude ( $A_1$ ) leads to the rise of C2's amplitude ( $A_2$ ) but the decrease of its relative amplitude ( $A_2/A_1$ ). The increase in  $A_1$  also slightly reduces the value of  $f_1$  at the maximum  $A_2$ . In addition, the vibration centre of C1 shifts away from the initial location in the cases with large gap ratio. The shift becomes increasingly obvious with an increase of  $A_1$  and  $f_1$ . Finally, C2 responds to the vibration of C1 with bigger amplitude in some situations with small gap ratios, which can be interpreted as the occurrence of resonance.

**Key words:** Vortex-induced vibration, computational fluid dynamics, resonance



# Table of contents

<b>List of figures</b>	<b>xi</b>
<b>List of tables</b>	<b>xiii</b>
<b>Nomenclature</b>	<b>xv</b>
<b>1 Introduction</b>	<b>1</b>
1.1 Motivation . . . . .	1
1.2 Objectives . . . . .	1
1.3 Outline of Report . . . . .	2
<b>2 Literature Review</b>	<b>5</b>
2.1 Vortex-induced Vibration of Single Cylinder . . . . .	5
2.1.1 Classic equations for cylinder oscillation . . . . .	6
2.1.2 Amplitude response types . . . . .	8
2.1.3 Critical mass ratio . . . . .	11
2.2 Flow around Two Cylinders . . . . .	15
2.3 Flow around Cylinder Arrays . . . . .	17
2.4 Summary . . . . .	21
<b>3 Numerical Method</b>	<b>23</b>
3.1 Governing Equations . . . . .	23
3.2 Finite Element Method . . . . .	24
3.3 Arbitrary Lagrangian-Eulerian Method . . . . .	26
3.4 Turbulence Modelling Strategies . . . . .	26
3.4.1 Direct numerical simulation . . . . .	27
3.4.2 Large eddy simulation . . . . .	28
3.4.3 Reynolds-averaged Navier–Stokes simulation . . . . .	29

<b>4 Numerical Results</b>	<b>31</b>
4.1 Case Setup . . . . .	31
4.2 Dimensional Analysis . . . . .	31
4.3 Mesh Independence Study . . . . .	33
4.4 Validation . . . . .	35
4.5 Cylinder-interaction Results . . . . .	37
4.6 Discussion . . . . .	42
4.7 Summary . . . . .	42
<b>5 Conclusion &amp; Future Plan</b>	<b>45</b>
5.1 Conclusion . . . . .	45
5.2 Future Plan . . . . .	46
<b>References</b>	<b>49</b>

# List of figures

2.1	(a) Added mass and (b) oscillation frequency for VIV of single cylinder in water with $m^* = 1.306$ and $\zeta = 0.015$ . (b) shows the mean oscillation frequency divided by natural frequency in still water (0.497 Hz) (sloped lines) and the mean oscillation frequency divided by the true natural frequency using the added mass from Figure 4(a) corresponding to the given reduced velocity (the horizontal lines). [9]	9
2.2	The scheme depicts two different types of amplitude response. (Vertical axes represent $A^*$ and horizontal axes represent $U^*$ .) The high- $(m^*\zeta)$ type of response discovered by Feng [11] has two branches (initial and lower), while the low- $(m^*\zeta)$ type of response by Khalak & Williamson [12] shows three branches (initial, upper and lower). The mode transitions are either hysteretic (H) or involve intermittent switching (I). Khalak & Williamson stated that the range of synchronization is controlled primarily by $m^*$ (when $m^*\zeta$ is constant), and the peak amplitudes are controlled principally by $m^*\zeta$ .	10
2.3	"Griffin" plot by Govardhan & Williamson [16] shows peak amplitude $A_{max}^*$ versus a combined mass-damping parameter $(m^* + C_A)\zeta$ . Symbols: +, Feng [11]; $\square$ , Hover et al.[20]; $\circ$ , Khalak & Williamson [12]; $\odot$ , Govardhan & Williamson [16]; —, Skop & Balasubramanian [21].	11
2.4	Distribution of the lower branch frequency ( $f_{lower}^*$ ) with x-axis being the mass ratio $m^*$ [16]. The Equation (2.12) shows great correspondence with the experimental data from several authors [16, 20, 12, 22], predicting a surge of $f_{lower}^*$ as $m^*$ decreases towards the critical mass ratio, $m_{crit}^* = 0.54$ .	12
2.5	The shaded area mark the synchronisation regime varying with $m^*$ . The equation for $U_{end}^*$ shows good coherence with the data from several researchers [16, 20, 12, 22]. Also, as $m^*$ drops towards $m_{crit}^* = 0.54$ , the synchronization regime is greatly extended, and ultimately approaches infinity when $m^*$ drops below $m_{crit}^*$ . [16]	12

2.6	Strouhal number as a function of Reynolds number for circular cylinders. Data from Lienhard [23] and Achenbach and Heinecke [24]. $S \approx 0.21(1 - 21/Re)$ for $40 < Re < 200$ , from Roshko [25]. (plot by Techet [26] from the VIV lecture note of MIT OCW ) . . . . .	13
2.7	The data of lower branch regimes with two different values of $m^*$ are almost on the same line with the x-axis being $(U^*/f^*)S$ , plotted by Khalak & Williamson [12]. Circular dots: $m^* = 1.19$ and $(m^* + C_A)\zeta = 0.0110$ ; triangular dots: $m^* = 8.63$ and $(m^* + C_A)\zeta = 0.0145$ . Solid symbols indicate the lower branch regimes. . . . .	13
2.8	Lower branch frequency response for low $m^*\zeta$ with different mass ratios, showing a nearly constant value for each specific $m^*$ .[16] . . . . .	14
2.9	Vorticity contours for two elastically mounted and rigidly connected cylinders in the side-by-side arrangement at $G = 3$ , $V_r = 5$ , $Re = 5000$ , $m^* = 2.5$ , $\zeta = 0$ . [49] . . . . .	17
2.10	Typical Row pattern in various arrangements (a) $\theta = 0^\circ$ , $3.94 < L_c/D$ ; (b) $\theta = 0^\circ$ , $1.70 < L_c/D < 3.94$ ; (c) $\theta = 0^\circ$ , $L_c/D < 1.70$ ; (d) $\theta = 10^\circ$ , $3.94 < L_c/D$ ; (e) $\theta = 10^\circ$ , $1.88 < L_c/D < 3.94$ ; (f) $\theta = 10^\circ$ , $L_c/D < 1.88$ ; (g) $\theta = 20^\circ$ , $2.40 < L_c/D$ ; (h) $\theta = 20^\circ$ , $1.28 < L_c/D < 2.40$ ; (i) $\theta = 20^\circ$ , $L_c/D = 1.28$ . $L_c$ = centre to centre spacing ; $\theta$ = flow incident angle. [50] .	18
2.11	Near field view of the vorticity field, $\omega_v$ , for the arrays (a) C1, (b) C7, (c) C20, (d) C39, (e) C64, (f) C95, (g) C133 and (h) CS1. $Re = 100$ for C1 and $Re = 2100$ for C7~C133. The colours red and blue denote positive and negative vorticity respectively, with green corresponding to irrotational fluid. The flow is directed from left to right. [62] . . . . .	19
2.12	Contours of the non-dimensional vorticity for VIV of the cylinder array for $L_c/D = 2$ , $Re = 100$ , $m^* = 2.5$ . ( $L_c$ = centre-to-centre distance) [63] . . . . .	20
4.1	Interaction between two cylinders: Cylinder 1 (C1) undergoes harmonic forced vibration while Cylinder 2 (C2) responds with 1DOF along y-axis with restoring force. . . . .	32
4.2	Computational mesh for two cylinders with $G=0.2$ . . . . .	34
4.3	The results of the mesh dependency study. . . . .	34
4.4	Single cylinder mesh for validation case with $N_c = 134$ and $\Delta r \approx 0.00183$ .	35
4.5	Comparison of fluid velocity distribution between the numerical simulation results and the experimental data by Dutsch [103] . . . . .	36

4.6	Comparison between Cylinder 1 and Cylinder 2's displacement histories at $G = 0.2, A_1 = 0.1, f_1 = 0.65, 0.8, 0.85, 0.9, 1.6, 2.0$ . The blue line denotes Cylinder 1, while red line denotes Cylinder 2. . . . .	38
4.7	(a) Variation of C2's response amplitude with the frequency of C1 for $G = 3, A_1 = 0.5, 1.0, 1.5, 2.0, 2.5$ , and (b) Variation of C2's amplification factor with the frequency of C1, for $G = 3, A_1 = 0.5, 1.0, 1.5, 2.0, 2.5$ . . . . .	39
4.8	(a) & (c) & (e) Variation of C2's amplification factor with the frequency of C1, for $G = 0.2, 1, 1.25; A_1 = 0.025, 0.05, 0.075, 0.1, 0.15, 0.2, 0.25, 1$ . (b) & (d) & (f) Close-up view near resonance. . . . .	40
4.9	Variation of maximum $A_2/A_1$ with the gap ratio $G$ , where the value of $A_1$ is always $G/2$ . . . . .	41
4.10	Displacement time histories of C2 . . . . .	41
4.11	Dependence of $\Delta\bar{Y}/A_2$ on $A_1$ & $f_1$ for $G=3$ . . . . .	43

## List of tables

2.1	Non-dimensional groups in literature review . . . . .	6
4.1	Non-dimensional groups to determine a case . . . . .	33
4.2	Computational meshes for various gap ratios . . . . .	35
5.1	Simulation Options . . . . .	46



# Nomenclature

## Acronyms

ALE Arbitrary Lagrangian-Eulerian method

C1 Cylinder 1 (forced vibration) for interaction between two cylinders

C2 Cylinder 2 (freely oscillating) for interaction between two cylinders

CFD Computational Fluid Dynamics

DEM Discrete Element Method

DNS Direct Numerical Simulation

DOF Degree Of Freedom

FEM Finite Element Method

FVM Finite Volume Method

HPC High-Performance Computing

ILES Implicit Large Eddy Simulation

LES Large Eddy Simulation

MILES Monotone Integrated Large Eddy Simulation

PDE Partial Differential Equations

RANS Reynolds-Averaged Navier-Stokes

VIV Vortex-Induced Vibration

VLES Very Large Eddy Simulation

### Greek Symbols

$\varepsilon$	Average dissipation rate of turbulence kinetic energy per unit mass	$[L]^2[T]^{-3}$
$\eta$	$= (\tilde{v}^3/\varepsilon)^{1/4}$ , kolmogorov length scale	
$\mu$	Dynamic viscosity of fluid	$N \cdot s/m^2$
$\omega$	$= 2\pi f$ , angular frequency	Hz
$\omega_t$	Specific rate of dissipation from turbulence kinetic energy into internal thermal energy	
$\omega_v$	Vorticity	
$\phi$	Phase angle difference between force and body oscillation	kg
$\phi_v$	Void fraction	
$\rho$	Density of fluid	$kg/m^3$
$\tilde{v}$	Kinematic viscosity of fluid	$[L]^2[T]^{-1}$
$\psi$	Phase of cylinder oscillation	
$\pi$	$\simeq 3.14159265358979323846264338327950288\dots$	

### Non-dimensional Parameters

$C_y$	Transverse force coefficient	$\frac{F}{0.5\rho U^2 D L}$
$f^*$	Frequency ratio	$\frac{f_{osc}}{f_{wn}}$
$Re$	Reynolds number (for flow conditions)	$\frac{\rho U D}{\mu}$
$\zeta$	Damping ratio (with added mass)	$\frac{c}{2\sqrt{k(m+m_A)}}$
$\nu$	Non-dimensional viscosity for interaction between two cylinders	$2\pi f_1 A_1 / Re_m$
$U^*$	Velocity ratio/ Reduced velocity/ Relative velocity defined by $f_{wn}$	$\frac{U}{f_{wn} D}$
$A_1$	Non-dimensional amplitude of Cylinder 1 (forced vibration)	$\frac{\tilde{A}_1}{D}$
$A_2$	Non-dimensional amplitude of Cylinder 2 (freely oscillating)	$\frac{\tilde{A}_2}{D}$

$f_1$	Non-dimensional frequency of Cylinder 1 (forced vibration)	$\frac{\tilde{f}_1}{f_n}$
$f_2$	Non-dimensional frequency of Cylinder 2 (freely oscillating)	$\frac{\tilde{f}_2}{f_n}$
$G$	Gap ratio	$\frac{\tilde{G}}{D}$
$p$	Pressure	$\tilde{p}/(\rho f_n^2 D^2)$
$t$	Non-dimensional time	$\tilde{t} f_n$
$u$	Non-dimensional horizontal fluid velocity	$v/(f_n D)$
$v$	Non-dimensional vertical fluid velocity	$u/(f_n D)$
$A^*$	Amplitude ratio	$\frac{A}{D}$
$\Delta r$	Non-dimensional element size along the radial direction	
$\Delta s$	Non-dimensional element size along the circumferential direction	
$\Delta t$	Non-dimensional time step	
$m^*$	Mass ratio (bluff body mass divided by displaced fluid mass)	$\frac{m}{\pi \rho D^2 L / 4}$
$Re_m$	Reynolds number regarding $U_{1m}$ for cylinder interaction in still water	$\frac{2\pi \tilde{A}_1 \tilde{f}_1 D}{\tilde{v}}$
$U_{1m}$	= $2\pi \tilde{A}_1 \tilde{f}_1$ Maximum oscillation velocity of Cylinder 1	$[L][T]^{-1}$
$V_r$	Velocity ratio/ Reduced velocity/ Relative velocity defined by $f_n$	$\frac{U}{f_n D}$

### Roman Symbols

$c$	Damping coefficient	$N \cdot s/m$
$C_{EA}$	Effective added mass coefficient	Hz
$D$	Cylinder diameter	m
$F$	Time-dependent resultant force induced by surrounding fluid	N
$f_{n,true}$	True natural frequency	Hz
$k$	Spring constant/ stiffness	N/m

---

$k_t$	Turbulence kinetic energy	
$L$	Axial length of cylinder	m
$M$	$= m/L$ , mass per unit span of bluff body	kg/m
$m$	Mass of bluff body	kg
$m_A$	Fluid added mass for bluff body oscillation	kg
$N$	Number of cylinders	
$N_c$	Element number along the boundary of a cylinder	$\frac{\tilde{A}_2}{D}$
$S$	Strouhal number for static cylinder	
$T$	Period of bluff body oscillation	s
$U$	Freestream velocity of fluid	m/s
$V_{cyl}$	Volume of a cylinder	$\text{m}^3$
$y$	Mass of bluff body	kg
$\Delta \bar{Y}$	Displacement of vibration centre	
$A$	Response amplitude for single cylinder VIV	m
$C_r$	Courant number in the radial direction along the boundary of a cylinder	
$C_s$	Courant number in the circumferential direction along the boundary of a cylinder	
$f_n$	$= \sqrt{k/m}/2\pi$ , undamped/ structural/ vacuum natural frequency	Hz
$f_{osc}$	Cylinder oscillation frequency	Hz
$f_{wn}$	$= \sqrt{k/(m+m_A)}/2\pi$ , natural frequency in still water	Hz

### Superscripts

$\ddot{y}$	$= d^2y/dt^2$	
$\dot{y}$	$= dy/dt$	
$\tilde{G}$	Gap distance (wide tilde denotes dimensional parameters)	

**Subscripts**

$A_{max}$  Maximum response amplitude

$f_{lower}$  Lower-branch frequency for single cylinder VIV

$$y_{rms} = \sqrt{(y_1^2 + y_2^2 + \dots + y_n^2) / n}, \text{ root mean square value}$$

$(A_2/A_1)_{peak}$  The maximum value from a series of  $A_2/A_1$

$m_{crit}^*$  critical mass ratio

$U_{end}^*$  End of the lower branch & synchronisation for single cylinder VIV

$U_{start}^*$  Start of the lower branch for single cylinder VIV



# **Chapter 1**

## **Introduction**

### **1.1 Motivation**

The motivation of this Ph.D. project is to mitigate negative impacts of multi-cylinder vortex-induced vibration (VIV) on structures such as heat exchangers, marine cables, chimneys, offshore pipelines bridges, and skyscrapers. Also, many real contexts of VIV problems often involve a cluster of cylindrical structures, and it is therefore necessary to investigate how the response of one cylinder affects the response of another in its wake [1] or, for further simplification, in still water. For example, typically in oil industry, vortex-induced vibration causes fatigue damage of offshore oil exploration or production risers. Both current flows and top-end vessel motions actuate these slender structures, and the vibrating structures also interact with each other by passing momentum through the fluid, giving rise to the flow-structure relative motion and causing VIV [2]. In addition, giant oil companies such as BP, ExxonMobil, and Shell are known to have supported the VIV research [3]. This study hopes to ultimately obtain a deeper understanding of the physics for interaction between fluid and multiple cylinders as well as conclusions valuable for engineering design optimisation.

### **1.2 Objectives**

For decades, VIV has been a classic topic in the field of fluid-structure interaction. However, VIV for both single cylinder and multi-cylinder are still to be fully understood and require further studies. Existing multi-cylinder research showed its limitation that all physical or numerical experiments were conducted under an external flow, and there has never been any study in still water. Also, it seems that current multi-cylinder investigation are constrained

to description of flow pattern and cylinder response modes, and are rather qualitative than quantitative compared with single cylinder VIV.

Consequently, during my first year, the problem investigated is the interaction between two cylinders immersed in otherwise still water: One cylinder (C1) undergoes forced vibration that disturbs the fluid, whereas another cylinder (C2), which has one-degree-of-freedom (1DOF), vibrates correspondingly under the action of the imbalanced hydrodynamic force. This configuration excludes the effects caused by the flow, which allows the investigation to focus on the mechanism of interaction between the two oscillating cylinders. A two-dimensional (2D) numerical model based on Navier-Stokes (NS) equations and finite element method (FEM) was applied to investigate the interaction between fluid and multiple cylinders in still water.

My investigation in the first year has focused on cases with constant Reynolds number  $Re_m = 100$  and mass ratio  $m^* = 2.5$ . The interpretation of results has concentrated on how the passive cylinder C2 responded to the oscillation of the actuating cylinder C1 through the induced fluid motion (see Section 4.7 for details), while the reasons of this response behaviour is still to be discussed in the future (see Section 5.2).

The objective of my future Ph.D. research is to further approach the engineering reality by the following ways and discuss the underlying physics. The degree of freedom (DOF) for responding cylinder will be increased from 1DOF to 2DOF. The 2D numerical model will be replaced by another 3D model to test the influence of 3D turbulent flows on the responding cylinder. Reynolds-averaged Navier–Stokes simulation (RANS) or large eddy simulation (LES) may be implemented instead of direct numerical simulation (DNS) to conduct affordable numerical simulations in high Reynolds number. At last, the flow condition may also be employed. In addition, the reason why fluid and cylinders interact in such a way will be discussed and compared with available theories.

## 1.3 Outline of Report

The remainder of this report is structured as follows:

- Literature Review (Chapter 2) summarises and reviews previous researches about flow-cylinder interaction of one (Section 2.1), two (Section 2.2), or more than two (Section 2.3) cylinders;
- Numerical Method (Chapter 3) explains the computational techniques related to the current numerical model (Sections 3.2–4) and presents the governing equations for the current model (Section 3.1);

- Numerical Results (Chapter 4) demonstrates simulation results with curious phenomena observed and useful conclusions discovered;
- Summary & Future Plan (Chapter 5) draws conclusion for the entire report and points out future research direction accompanied by a Gantt chart.



# **Chapter 2**

## **Literature Review**

This research investigates the interaction between fluid and multiple cylinders, which is most often placed in the context of multi-cylinder vortex-induced vibration (VIV). This literature review, therefore, lays emphasis on the vortex-induced vibration for both single and multiple cylinders.

Vortex-induced vibration (VIV) accounts for disastrous failures in various engineering applications, including aero, civil, mechanical, marine, offshore, and nuclear engineering. Ever since Leonardo da Vinci first observed VIV in 1504AD, in the form of "Aeolian Tones," engineers have spared no effort on investigating VIV to mitigate its damaging effects [4]. VIV of a bluff body exposed to a flow is a result of vortex formation and shedding on the downstream side the body. Vortex shedding alternates from one side to another, causing oscillations or even the torsional vibrations of elastic bodies (e.g. cylinders, spheres). This fluid-structure interaction phenomenon occurs as a result of lock-in, i.e. synchronisation between vortex shedding and bluff body oscillation, due to non-linear resonance of cylinders (or spheres). This chapter summarises the most significant research for single cylinder VIV, as well as that for multi-cylinder VIV.

### **2.1 Vortex-induced Vibration of Single Cylinder**

This section discusses flow-induced vibration of a freely oscillating elastically mounted cylinder with 1-Degrees-Of-Freedom (1DOF). Table 2.1 lists the frequently used non-dimensional groups throughout this chapter.

Table 2.1 Non-dimensional groups in literature review

Mass ratio	$m^*$	$\frac{m}{\pi\rho D^2 L/4}$
Damping ratio (with added mass)	$\zeta$	$\frac{c}{2\sqrt{k(m+m_A)}}$
Velocity ratio	$U^*$	$\frac{U}{f_{wn}D}$
Amplitude ratio	$A^*$	$\frac{A}{D}$
Frequency ratio	$f^*$	$\frac{f}{f_{wn}}$
Transverse force coefficient	$C_y$	$\frac{F}{0.5\rho U^2 D L}$
Reynolds number	$Re$	$\frac{\rho U D}{\mu}$

### 2.1.1 Classic equations for cylinder oscillation

Several equations have been commonly used in the investigation of a cylinder's vortex-induced vibration (VIV), describing the motion of a cylinder and the forces upon it. Equation (2.1) is used to describe the motion of cylinder in the Y (transverse) direction:

$$m\ddot{y} + c\dot{y} + ky = F(t) \quad (2.1)$$

where  $m$  is the mass of cylinder,  $y$  is the displacement of the body,  $c$  is the structural damping coefficient,  $k$  is the spring's stiffness constant, and  $F(t)$  is the time-dependent force induced by the surrounding fluid [5]. Furthermore, it is common to rewrite Equation (2.1) as Equation (2.2):

$$M\ddot{y} + 4\pi f_n \zeta M\dot{y} + 4\pi^2 f_n^2 My = C_y \rho U^2 D / 2 \quad (2.2)$$

where  $M = m/L$  is the mass per unit span,  $\zeta$  is the damping ratio,  $f_n = (k/M)^{1/2}/2\pi$  is the undamped natural frequency (also termed as "structural natural frequency" [6]),  $C_y = F(t)/0.5\rho U^2 D$  is the lift force coefficient (sometimes written as  $C_L$  [7]).  $C_y$  reflects the transverse direction component of the resultant instantaneous fluid force upon the oscillating bluff body, and includes parts considered as damping forces and fluid inertia.

Furthermore, provided that synchronisation (lock-in) between vortex wake and the cylinder's oscillation occurs, Equations (2.3) and (2.4) are suitable representations of the force

coefficient ( $C_y$ ) and the response ( $y$ ):

$$C_y(t) = C_{y_0} \sin(\omega t + \phi) \quad (2.3)$$

$$y(t) = A \sin(\omega t) \quad (2.4)$$

where  $\omega$  is equivalent to  $2\pi f$  and  $f$  is the actual frequency of cylinder's oscillation;  $C_{y_0}$  and  $A$  are the amplitude of force coefficient and body oscillation, respectively; and  $\phi$  is the phase angle difference between force and body oscillation.

Equations (2.5) and (2.6) can be deducted from Equations (2.2–4) (see ?? for details), as described by Bearman [5]:

$$\frac{f_{osc}}{f_n} = [1 - \frac{C_{y_0}}{4\pi^2} \cos\phi \frac{\rho D^2}{2M} (\frac{U}{f_n D})^2 \frac{D}{y}]^{1/2} = \sqrt{\frac{m^*}{m^* + C_{EA}}} \quad (2.5)$$

$$\frac{A}{D} = \frac{1}{4\pi^3} \frac{C_{y_0} \sin\phi}{m^* \zeta} (\frac{U}{f D})^2 \frac{f_{osc}}{f_n} \quad (2.6)$$

while Williamson [8] transformed Equations (2.5) and (2.6) into Equations (2.7) and (2.8) by the fact that  $f_{wn}/f_n = \sqrt{m^*/(m^* + C_A)}$ :

$$f^* = \frac{f_{osc}}{f_{wn}} = \sqrt{\frac{m^* + C_A}{m^* + C_{EA}}} \quad (2.7)$$

$$A^* = \frac{A}{D} = \frac{1}{4\pi^3} \frac{C_{y_0} \sin\phi}{(m^* + C_A) \zeta} (\frac{U}{f D})^2 \frac{f_{osc}}{f_{wn}} \quad (2.8)$$

where  $C_{EA}$  is the effective added mass coefficient as seen in Equation (2.9):

$$C_{EA} = \frac{1}{2\pi^3} \frac{C_{y_0} \cos\phi}{A/D} (\frac{U}{f_{osc} D})^2 \quad (2.9)$$

The form of Equations (2.7) and (2.8) is slightly different from Equations (2.5) and (2.6) in that the added mass,  $C_A$ , is utilised ( $C_A \approx 1.0$  for a circular cylinder), and the undamped natural frequency (in vacuum)  $f_n$  is replaced by the natural frequency in still water ( $f_{wn}$ ).

Moreover, some issues were encountered with the application of added mass  $m_A$  and the natural frequency  $f_n$  in these equations. The true natural frequency  $f_{n,true}$  is actually not a constant but varies according to the fluid added mass of the oscillating cylinder [9]:  $f_{n,true} \xrightarrow{\text{depends on}} m_A$ . The oscillation frequency  $f_{osc}$ , and therefore probably also  $m_A$ , is known to depend on reduced velocity  $U^* = U/f_n D$ , for cylinders with low mass ratio[10]:  $m_A \xrightarrow{\text{depends on}} f_{osc} \xrightarrow{\text{depends on}} U^* \xrightarrow{\text{depends on}} f_{n,true}$ . As we can see, here emerges a circular problem which is usually solved by predefining the value of  $f_n$ . For example, it is often

prescribed as the natural frequency measured in still water  $f_{wn}$  [8, 9], corresponding to  $C_A(f_{wn}) = 1.04$ .

Vikestad *et al.* [9] carried out a series of experiments to measure the true natural frequency  $f_n(U_r)$ , which was calculated as Equations (2.10) and (2.11):

$$C_A = -\frac{8}{nT\rho\pi D^2L(\omega^2A)^2} \int_t^{t+nT} F\ddot{y}dt \quad (2.10)$$

$$f_{n,true}(U_r) = \frac{1}{2\pi} \sqrt{\frac{k}{m + \rho V_{cy1} C_A(U_r)}} \quad (2.11)$$

where  $\omega^2A = \sqrt{2}\ddot{y}_{rms}$ ,  $nT$  is an integer number  $n$  of oscillation periods  $T$ .

The added mass and mean oscillation as a function of non-dimensional velocity is plotted in Figure 2.1 [9]. The mean oscillation frequency in Figure 2.1b was computed as  $\sqrt{\ddot{y}_{rms}/y_{rms}}/(2\pi)$ . As seen in the figure, the added mass coefficient  $C_A$  drops monotonically with non-dimensional flow speed  $U^*$ , causing the true natural frequency  $f_{n,true}$  to increase as well.

### 2.1.2 Amplitude response types

The response types of an elastically mounted cylinder can be classified into two types by the combined mass-damping parameter ( $m^*\zeta$ ), as stated by Khalak & Williamson [12]. Feng [11] conducted a pioneering experimental study regarding an elastically mounted cylinder with high mass-damping parameter ( $m^*\zeta \approx 0.25$ ). Feng found two dissimilar branches regarding amplitude response, which were afterwards termed by Khalak & Williamson as the "initial branch," where the highest amplitudes are reached, and the "lower branch" (see Figure 2.2a). Later experiments for a long flexible circular cylinder at high  $m^*\zeta$  conducted by Brika & Laneville [13] confirmed the existence of the two-branch amplitude response. A hysteresis loop between initial & lower branches was observed in both experiments (see the "H" in Figure 2.2a), yet Brika & Laneville's hysteresis loop (for a long flexible cylinder) was partially different from this illustration. Regarding low  $m^*\zeta \approx 0.013$ , Khalak & Williamson's experiments [12, 14, 15] identified three branches of response (see Figure 2.2b). An extra "upper branch" was discovered in addition to the initial & lower branch. Also, two transitions were identified between these three branches: the hysteretic transition between the initial and upper branches, and the intermittent transition between the upper and lower branches.

The distribution of maximum amplitude  $A_{max}^*$  versus the combined mass-damping parameter  $(m^* + C_A)\zeta$  (usually called a "Griffin" plot) is demonstrated in Figure 2.3 [16], where "Upper" denotes the maximum amplitudes of upper branches, while "Lower" denotes those of

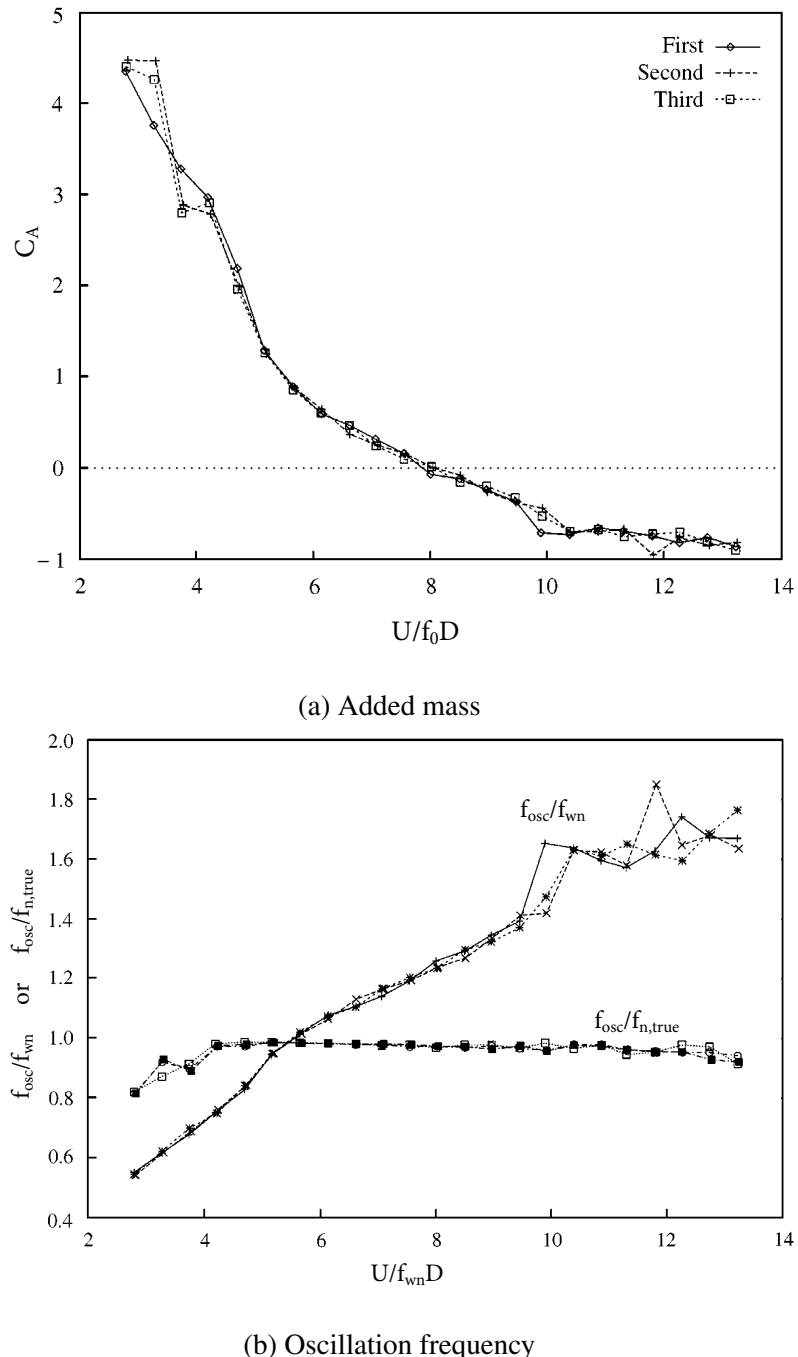


Fig. 2.1 (a) Added mass and (b) oscillation frequency for VIV of single cylinder in water with  $m^* = 1.306$  and  $\zeta = 0.015$ . (b) shows the mean oscillation frequency divided by natural frequency in still water (0.497 Hz) (sloped lines) and the mean oscillation frequency divided by the true natural frequency using the added mass from Figure 4(a) corresponding to the given reduced velocity (the horizontal lines). [9]

the lower branches. A curve line standing for a semi-empirical equation is drawn to compare with some experimental data. The equation aims to represent the vibration of spring-mounted, pivoted or cantilevered cylinders, as well as taut cables, and was compiled originally by Griffin [17] in 1980, and then updated by Skop & Balasubramanian [18] in 1997. Govardhan & Williamson reported that, for strictly elastically mounted bluff bodies, some data of  $A_{max}^*$  deviate from the curve. This deviation is possibly because the cases with  $Re \leq 200$  are not considered by the curve, as supported by experimental results from Anagnostopoulos & Bearman [19].

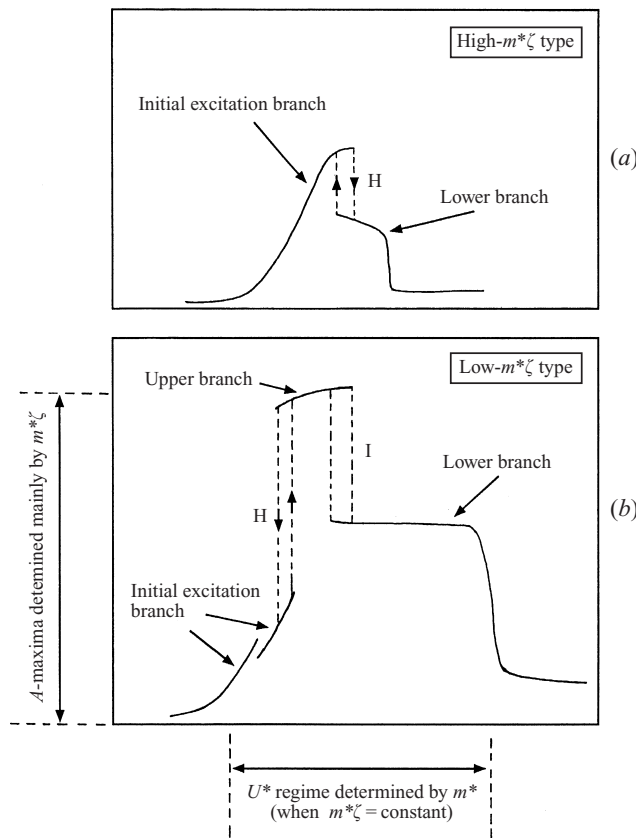


Fig. 2.2 The scheme depicts two different types of amplitude response. (Vertical axes represent  $A^*$  and horizontal axes represent  $U^*$ .) The high- $(m^*\zeta)$  type of response discovered by Feng [11] has two branches (initial and lower), while the low- $(m^*\zeta)$  type of response by Khalak & Williamson [12] shows three branches (initial, upper and lower). The mode transitions are either hysteretic (H) or involve intermittent switching (I). Khalak & Williamson stated that the range of synchronization is controlled primarily by  $m^*$  (when  $m^*\zeta$  is constant), and the peak amplitudes are controlled principally by  $m^*\zeta$ .

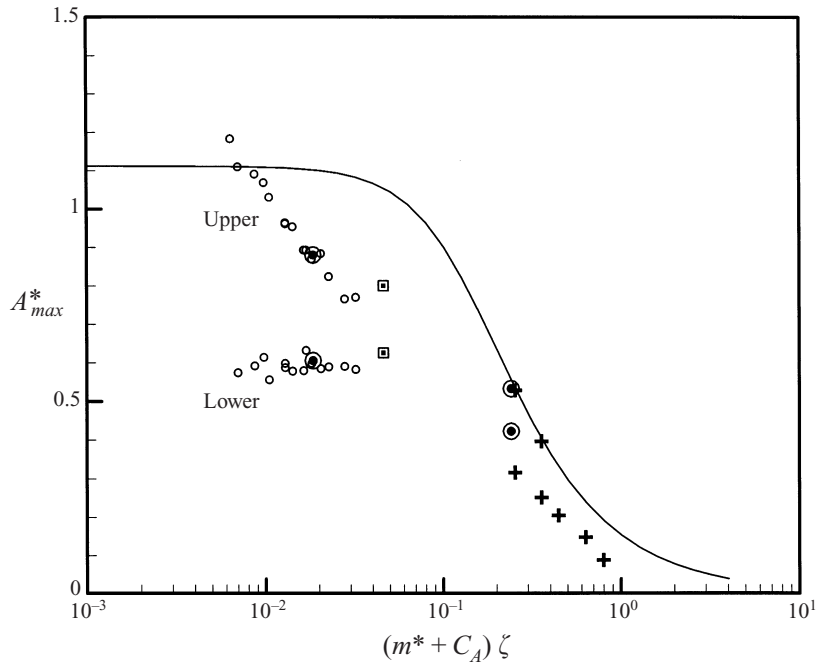


Fig. 2.3 "Griffin" plot by Govardhan & Williamson [16] shows peak amplitude  $A^*_{max}$  versus a combined mass-damping parameter  $(m^* + C_A)\zeta$ . Symbols: +, Feng [11];  $\square$ , Hover et al.[20];  $\circ$ , Khalak & Williamson [12];  $\odot$ , Govardhan & Williamson [16];—, Skop & Balasubramanian [21].

### 2.1.3 Critical mass ratio

A critical mass ratio for low mass-damping ratio, (broadly  $(m^* + C_A)\zeta < 0.05$ ), was firstly discovered by Govardhan & Williamson [16], who summarised the behaviour of lower branch frequency ( $f_{lower}^* = f_{lower}/f_{wn}$ ) from experimental data from several authors: Govardhan & Williamson [16], Hover et al. [20], Khalak & Williamson [12], and Anand [22]. By observing the collapse of these experimental data (see Figure 2.4), Govardhan & Williamson [16] concluded that if the mass-damping ratio is low, the value of  $f_{lower}^*$  depends solely on  $m^*$ . Moreover, as the cylinder's oscillation syncs with the vortex shedding in lower branch regime, fulfilling the prerequisite of equations Equations (2.3) and (2.4), they stated that Equation (2.7) is applicable, and the value of effective added mass ( $C_{EA}$ ) in Equation (2.9) depends merely on  $\{(U^*/f^*)S, A^*\}$ , where  $U^* = U/f_n D$ . The Strouhal number for static cylinder  $S$  is approximately 0.2 because all the experiments mentioned were carried out within the range of  $Re \in [200, 10^5]$  (see Figure 2.6). Also, as shown in Figure 2.7, despite the variation of  $m^*$  and  $(m^* + C_A)\zeta$ , all lower branch data (solid symbols) were plotted along the same line, meaning the variation of  $m^*$  does not affect the functional relationship between

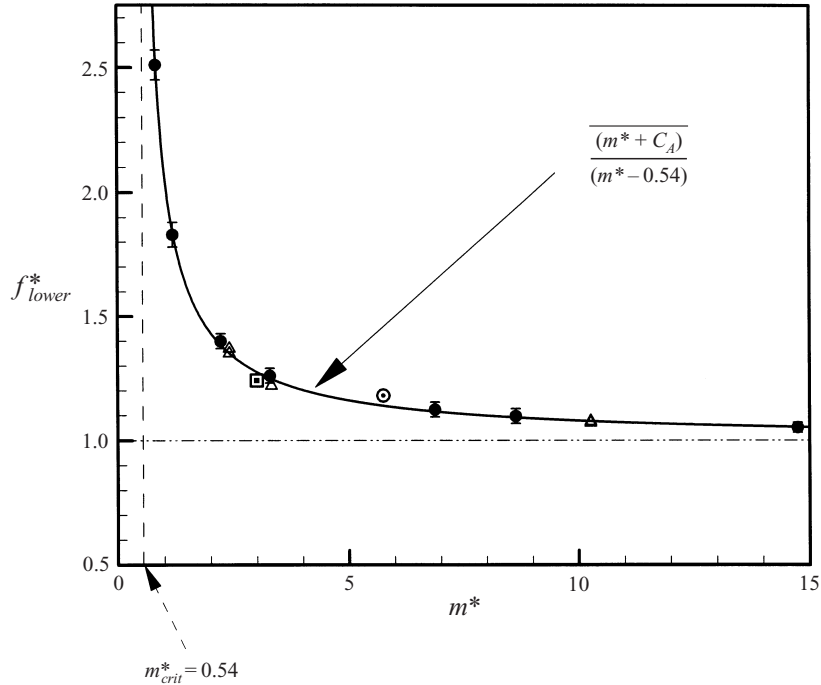


Fig. 2.4 Distribution of the lower branch frequency ( $f_{lower}^*$ ) with x-axis being the mass ratio  $m^*$  [16]. The Equation (2.12) shows great correspondence with the experimental data from several authors [16, 20, 12, 22], predicting a surge of  $f_{lower}^*$  as  $m^*$  decreases towards the critical mass ratio,  $m_{crit}^* = 0.54$ .

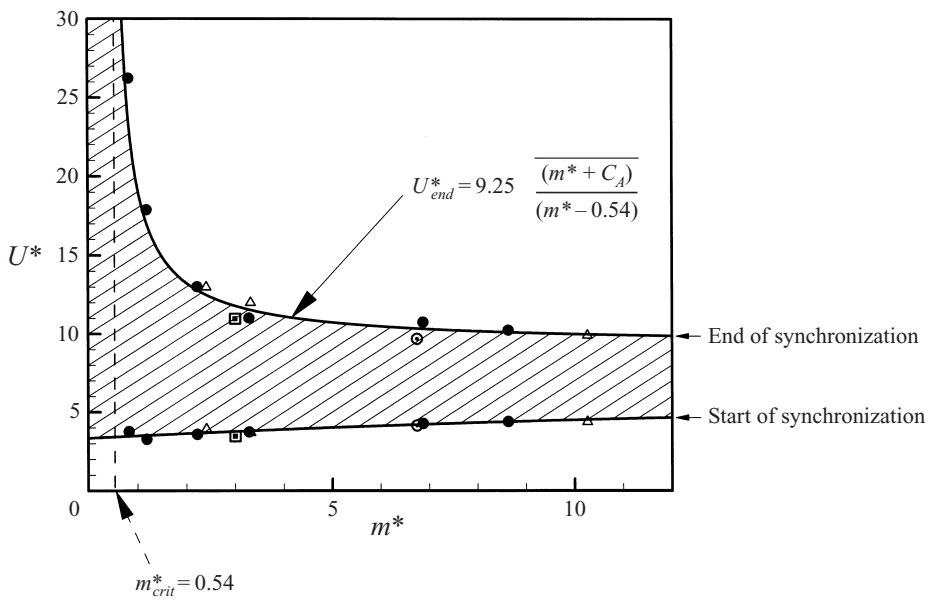


Fig. 2.5 The shaded area mark the synchronisation regime varying with  $m^*$ . The equation for  $U_{end}^*$  shows good coherence with the data from several researchers [16, 20, 12, 22]. Also, as  $m^*$  drops towards  $m_{crit}^* = 0.54$ , the synchronization regime is greatly extended, and ultimately approaches infinity when  $m^*$  drops below  $m_{crit}^*$ . [16]

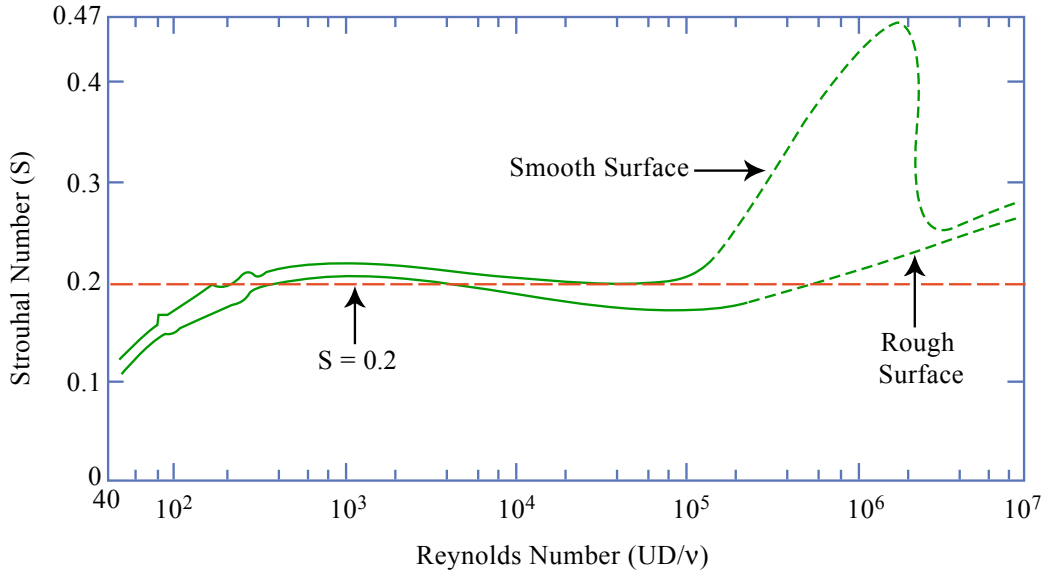


Fig. 2.6 Strouhal number as a function of Reynolds number for circular cylinders. Data from Lienhard [23] and Achenbach and Heinecke [24].  $S \approx 0.21(1 - 21/Re)$  for  $40 < Re < 200$ , from Roshko [25]. (plot by Techet [26] from the VIV lecture note of MIT OCW )

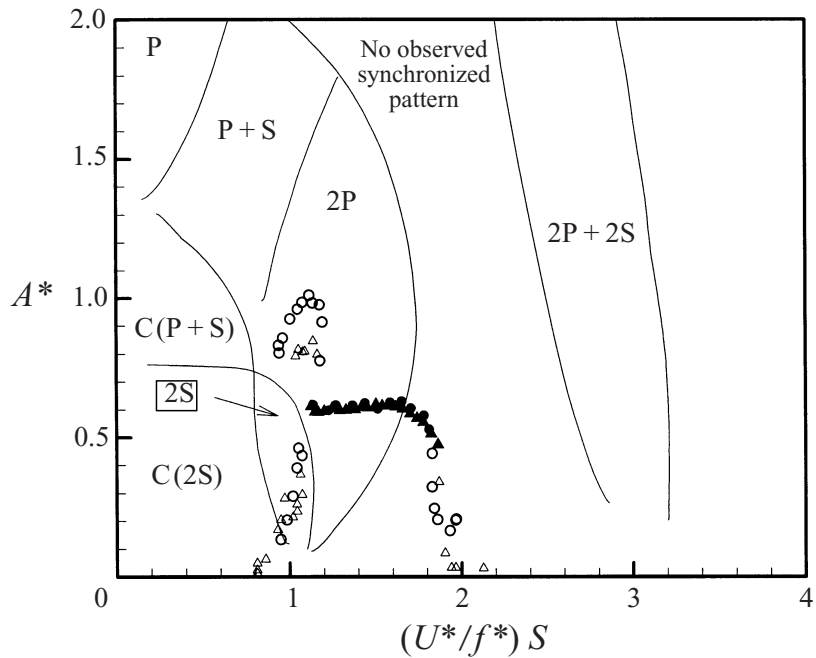


Fig. 2.7 The data of lower branch regimes with two different values of  $m^*$  are almost on the same line with the x-axis being  $(U^*/f^*)S$ , plotted by Khalak & Williamson [12]. Circular dots:  $m^* = 1.19$  and  $(m^* + C_A)\zeta = 0.0110$ ; triangular dots:  $m^* = 8.63$  and  $(m^* + C_A)\zeta = 0.0145$ . Solid symbols indicate the lower branch regimes.

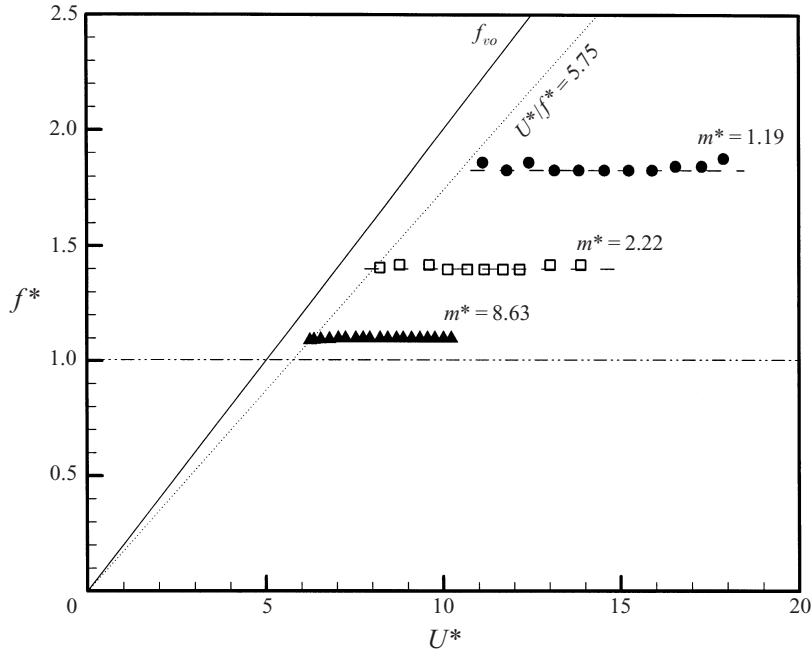


Fig. 2.8 Lower branch frequency response for low  $m^* \zeta$  with different mass ratios, showing a nearly constant value for each specific  $m^*$ .[16]

$(U^*/f^*)S$  and  $A^*$ , thus not affecting the value of  $C_{EA}$ . In other words, for lower branch,  $C_{EA}$  is a constant in Equation (2.7).

By fitting experimental data, they found the value of  $C_{EA}$  to be  $C_{EA} = -0.54 \pm 0.02$ , thus producing Equation (2.12):

$$f_{lower}^* = \frac{f_{lower}}{f_{wn}} = \sqrt{\frac{m^* + C_A}{m^* - 0.54}} \quad (2.12)$$

where  $C_A = 1.0$ . Equation (2.12) is plotted in Figure 2.4, having good correspondence with the several sets of experimental data. The equation offers a practical prediction to cylinder's lower branch frequency ( $f_{lower}^*$ ), provided that the mass ratio ( $m^*$ ) is given, and the mass-damping ratio is low (broadly  $(m^* + C_A)\zeta < 0.05$ ). Also, the critical mass ratio was determined as  $m_{crit}^* = 0.54$ .

In addition, as demonstrated in Figure 2.8, a relationship was summarised from 3 groups of experimental data in Equation (2.13):

$$U_{start}^* = 5.75 f_{start}^* = 5.75 f_{lower}^* \quad (2.13)$$

where the numerical value "5.75" has the experimental accuracy of  $\pm 0.2$ , and  $U_{start}^*$  is the start of the lower branch.

With equations Equations (2.12) and (2.13), they [16] further deduced that the start of lower branch regime (regarding reduced flow velocity,  $U^*$ ) can be formulated as Equation (2.14):

$$U_{start}^* \approx 5.75 \sqrt{\frac{m^* + C_A}{m^* - 0.54}} \quad (2.14)$$

From Equation (2.14), it can be seen that  $m^* \rightarrow m_{crit}^*$  results in  $U_{start}^* \rightarrow \infty$ . They consequently concluded that when mass ratio is below  $m_{crit}^* = 0.54$ , the lower branch will no longer exist, and the synchronisation will not cease with the increase of  $U^*$  (see Figure 2.5).

What is more, with similar process, the function to describe the end of lower branch regime — which is also the end of synchronisation regime — can be expressed as Equation (2.15):

$$U_{end}^* \approx 9.25 \sqrt{\frac{m^* + C_A}{m^* - 0.54}} \quad (2.15)$$

To summarise this section, Govardhan & Williamson [16] provided an experimentally supported method to predict both the start and the end of the lower branch regime using merely  $m^*$ , and discovered a critical mass ratio of  $m^* = 0.54$ . However, it is noteworthy that there are two prerequisites for the prediction equations: low mass-damping ratio (broadly  $(m^* + C_A)\zeta < 0.05$ ) and Reynolds number  $Re \in [200, 10^5]$  (thus  $S \approx 0.2$ ). Whether those equations are valid in other conditions appears to remain unchecked. In addition, it is not clearly explained why the effective added mass  $C_{EA}$  (see Equation (2.9)) is a function of  $\{(U^*/f^*)S, A^*\}$  (see Figure 2.7), which is not self-evident, although the final equations match well with the experimental data.

## 2.2 Flow around Two Cylinders

Two closely placed stationary circular cylinders with identical diameters exposed to flow are the most basic case for flow interaction with multiple cylindrical structures, which has been studied extensively in the past decades [27–29]. This section reviews previous studies for both two stationary & elastically mounted cylinders.

The most common configurations for two stationary cylinders are the side-by-side arrangement and tandem arrangement. For two cylinders in the side-by-side arrangement, it was found that the gap between the cylinders is an important factor for the flow pattern. If the gap between two cylinders is small, they behave as a single bluff body followed by a single wake [30, 31]. While the gap between cylinders is from  $0.1D$  to  $1.2D$  ( $D$  is the diameter of each cylinder), the biased flow occurs for certain experimental conditions and the Reynolds number, producing a wide wake behind one cylinder and a narrow wake behind another

[27, 30, 32]. In the subcritical Reynolds number regime, the direction of the biased flow changes randomly with time. For two cylinders in tandem arrangement, if the gap is less than  $2D$  to  $2.5D$  depending on the Reynolds number, the vortex shedding from the upstream cylinder is suppressed [33–35].

In terms of VIV for elastically mounted cylinders, studies were carried out for stationary cylinder and a downstream flexible cylinder, and it was found that responses of two riser pipes are categorised into two types: wake induced oscillation (i.e. galloping) and VIV [36, 37]. Furthermore, for two cylinders (both elastically mounted) in a side-by-side arrangement, the interference between them is very weak if the centre-to-centre distance surpasses 3.5 times the cylinder diameter [38]. In terms of numerical studies, VIV of two cylinders in tandem were mainly simulated at relatively low Reynolds numbers ( $Re \leq 1000$ ) [39–44]. Numerical simulations for the galloping responses of square cylinders also focused on low Reynolds numbers [44, 45]. For VIV of two rigidly connected cylinders with different diameters, experimental [46] and numerical [47] studies have been carried out motivated by the piggyback pipeline in offshore engineering, and the small cylinder in the proximity of the large cylinder was found to have great impact on the oscillation and vortex wake of the large cylinder.

Another classic configuration for VIV study is two identical rigidly connected cylinders with 1DOF, which is to investigate a bundle of pipelines or risers subjected to flows in natural environment. Considering the numerical simulation at low Reynolds number ( $Re = 150$ ), low mass ratio ( $m^* = 2.0$ ), and no damping ( $\zeta = 0$ ) [48], for side-by-side arrangement, a combination of VIV and galloping is found to occur at  $L/D = 1.5$  and 2. For tandem arrangement, the critical gap for the onset of vortex shedding from the upstream cylinder is significantly less than that for two stationary cylinders, while the critical gap is slightly greater than that at high Reynolds numbers.

In terms of high Reynolds number ( $Re = 5000$ ), low mass ratio ( $m^* = 2.5$ ), no damping ( $\zeta = 0$ ) using RANS model [49], for side-by-side arrangement, the maximum response amplitude was found to occur at  $G = 0.5$ , which is roughly twice the amplitude for that of the single cylinder VIV. It is interesting that for  $G = 1.5, 2, 2.5$ , and 3, the response amplitude was reported to be zero as the reduced velocity goes beyond 7, 6, 6, and 6.5, respectively, as the vortex shedding for each of two cylinders are out of phase with each other. For the tandem arrangement, the response amplitude for two cylinders is larger than that of a single cylinder for  $G = 0.5 \sim 2.5$ . In addition, the phenomenon of asymmetric vortex shedding is observed as seen in Figure 2.9.

In summary of this section, it can be seen that, despite useful conclusions found and interesting phenomena discovered, only a limited number of experimental or numerical

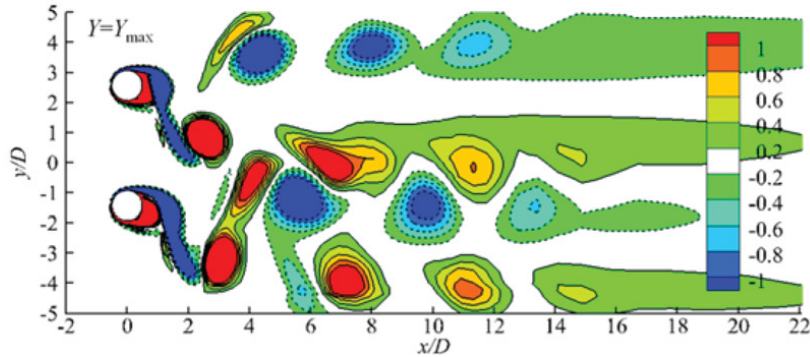


Fig. 2.9 Vorticity contours for two elastically mounted and rigidly connected cylinders in the side-by-side arrangement at  $G = 3$ ,  $V_r = 5$ ,  $Re = 5000$ ,  $m^* = 2.5$ ,  $\zeta = 0$ . [49]

studies were carried out regarding the investigation of two-cylinder cases, especially the elastically mounted and rigidly connected two cylinders in high Reynolds condition, where quantitative relationships between the inputted experimental configurations (e.g. gap ratio) and the outputted simulation results (e.g. vorticity contours) have not already been constructed. In addition, all the two-cylinder cases reviewed are exposed to moving fluid - none in still water, so there is clearly a need for more research in this area. See Chapter 4 for more details of what I have done.

## 2.3 Flow around Cylinder Arrays

Compared with flow around two cylinders, cases with flow around cylinder arrays is more complicated and closer to the engineering reality (e.g. cylinder arrays in heat exchangers). On the whole, interaction between flow and multiple cylinders was sensitive to the cylinders' arrangement and the distance between each cylinder [51]. This section summarises literature for both stationary & elastically mounted cylinder arrays.

Four stationary cylinders in a square arrangement exposed to a steady flow have been investigated in many studies (e.g. see Figure 2.10). The wake surrounding a four-cylinder array is much more complicated than that in previously mentioned one or two cylinders [52]. It was experimentally found that [53], at subcritical  $Re = 30000$ , the orientation of the cylinder group (regarding the direction of inlet flow) had significant impact on drag and lift coefficients upon each cylinder. For both three and four equispaced cylinders, minor modifications in the cylinder group orientation can result in significant changes in vortex shedding frequency. Moreover, for certain combinations of spacing ratios and flow inclination angles, the vortex shedding can be asymmetrical or even absent [54]. Lam & Lo [50] carried out flow visualization studies in inline & staggered square arrangements

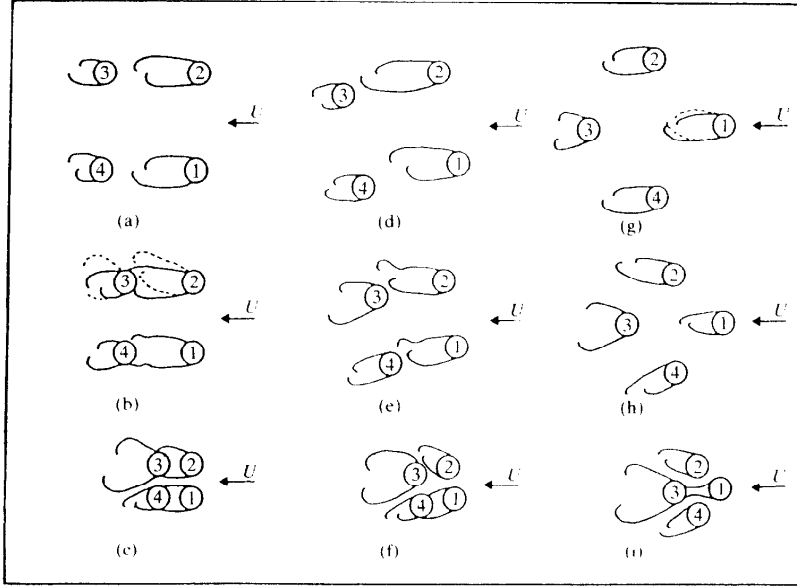


Fig. 2.10 Typical Row pattern in various arrangements (a)  $\theta = 0^\circ$ ,  $3.94 < L_c/D$ ; (b)  $\theta = 0^\circ$ ,  $1.70 < L_c/D < 3.94$ ; (c)  $\theta = 0^\circ$ ,  $L_c/D < 1.70$ ; (d)  $\theta = 10^\circ$ ,  $3.94 < L_c/D$ ; (e)  $\theta = 10^\circ$ ,  $1.88 < L_c/D < 3.94$ ; (f)  $\theta = 10^\circ$ ,  $L_c/D < 1.88$ ; (g)  $\theta = 20^\circ$ ,  $2.40 < L_c/D$ ; (h)  $\theta = 20^\circ$ ,  $1.28 < L_c/D < 2.40$ ; (i)  $\theta = 20^\circ$ ,  $L_c/D = 1.28$ .  $L_c$  = centre to centre spacing ;  $\theta$  = flow incident angle. [50]

at subcritical  $Re = 2100$ , and identified several distinct flow patterns (see Figure 2.10). Furthermore, in subsequent studies [55, 52, 56], the flow pattern was reported to have significant effects on the pressure distributions and the force coefficients. Flow patterns were found to change according to spacing ratios [57, 58], meanwhile digital particle image velocimetry and numerical simulations were also applied to investigate this problem. For an inline arrangement, the vortex shedding mode was in-phase at small spacing ratios and anti-phase at large spacing ratios [59]. Three types of flow patterns were found at  $Re = 200$  [60]: when the spacing ratio is small, the wake flow resembles a single-bluff body flow pattern; when the spacing ratio is 1.6, wiggling shielding wake was observed; when the spacing ratio was 3.5-4.0, four vortex streets were observed. Three dimensional numerical simulations were carried out for an inline arrangement simulated [61]. At a spacing ratio of 2 and  $Re = 100 \sim 500$ , four flow regimes were distinguished and a significant effect on the force was discovered in transitions between the flow regimes.

For stationary arrays with cylinder number  $N > 4$  (e.g. see Figure 2.11), greater complexity was encountered. Nicolle *et al.* [62] carried out two-dimensional numerical simulations for arrays with  $7 \sim 133$  cylinders, and found that the flow field through and around the cylinder group had strong correlation with the void fraction  $\phi_v$  (i.e. indicating density of the

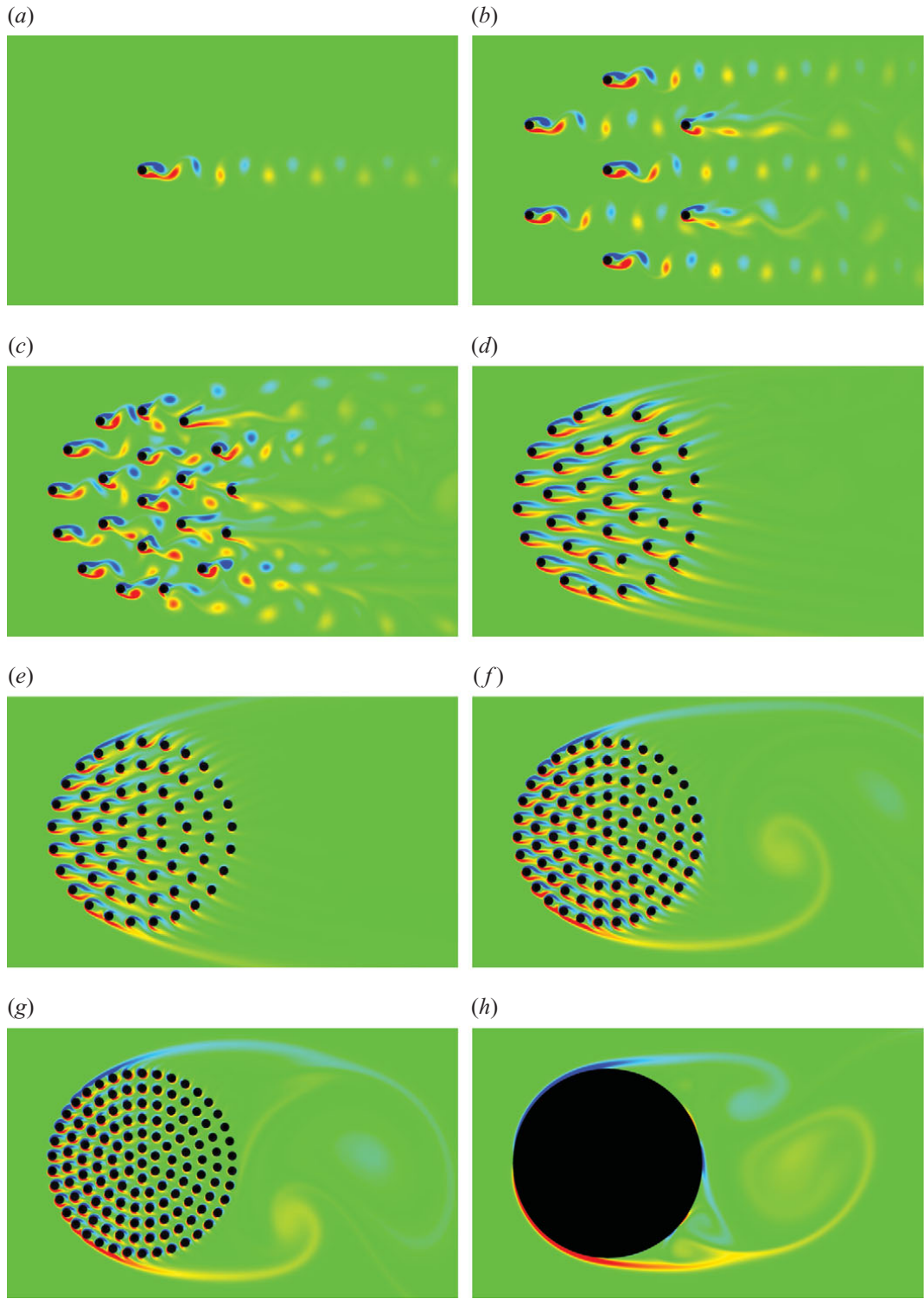


Fig. 2.11 Near field view of the vorticity field,  $\omega_v$ , for the arrays (a) C1, (b) C7, (c) C20, (d) C39, (e) C64, (f) C95, (g) C133 and (h) CS1.  $Re = 100$  for C1 and  $Re = 2100$  for C7~C133. The colours red and blue denote positive and negative vorticity respectively, with green corresponding to irrotational fluid. The flow is directed from left to right. [62]

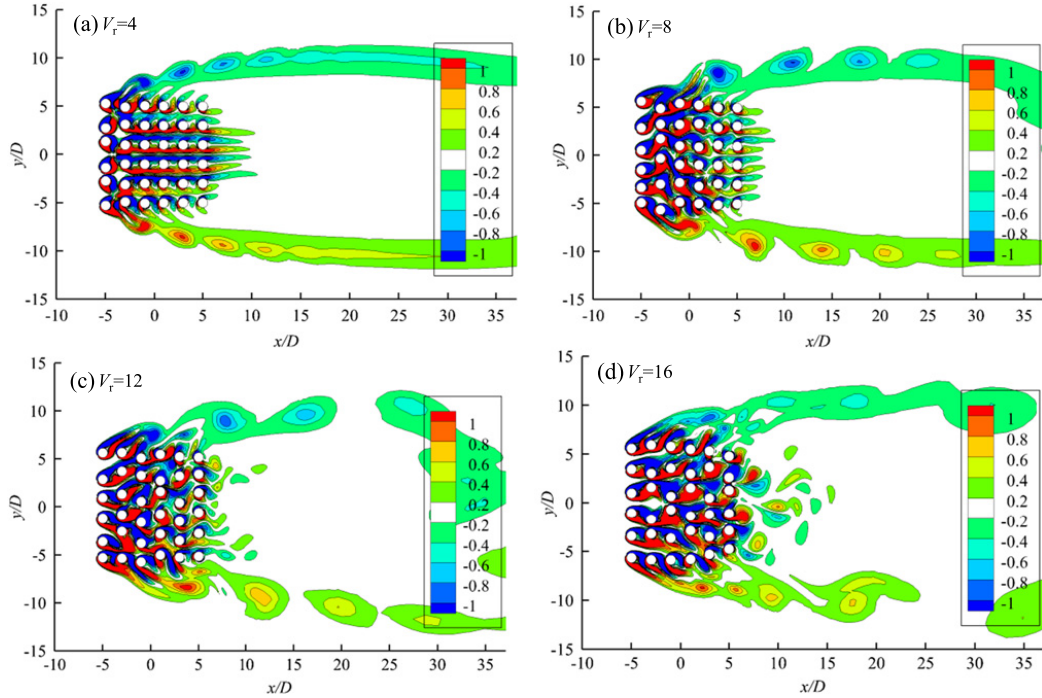


Fig. 2.12 Contours of the non-dimensional vorticity for VIV of the cylinder array for  $L_c/D = 2$ ,  $Re = 100$ ,  $m^* = 2.5$ . ( $L_c$  = centre-to-centre distance) [63]

cylinder group). As seen in Figure 2.11, for sufficiently small void fractions ( $\phi_v < 0.05$ ), the cylinders had uncoupled individual wake patterns, where the vorticity is rapidly dissipated by wake intermingling downstream. For moderate void fractions ( $0.05 < \phi_v < 0.15$ ), the wake flow was stable and force on the cylinder array was steady. For high void fractions ( $\phi_v > 0.15$ ), the wake behind the array was similar to a solid body of the same scale. Yu *et al.* [64] simulated flow through a circular array of cylinders (similar to the configuration from Nicolle [62]) in Reynolds numbers range 100 to 2000 using a hybrid RANS/LES turbulence model. They discovered that the drag coefficient increased with the void fraction, and was inversely correlated with Reynolds number. It was also found that the drag coefficient was independent of the cylinder array's diameter, when the void fraction and the Reynolds number were kept constant. Sweeney and Meskell [65] developed a fast discrete vortex method to simulate flow past cylinder arrays at  $Re = 2200$ . Their numerical result of Strouhal number was coherent with the previous data and the vortex shedding pattern qualitatively agreed with the flow visualization. The generation of three-dimensional vorticity was studied for flow past a square array of nine tubes with spacing ratios of 1.5 [66]. It was found that at  $Re = 200$  the three-dimensional instability was completely suppressed by tube's forced vibration, while at  $Re = 1000$  tube's forced vibration does not suppress the three-dimensional instability, yet

the flow's spanwise correlation was increased and the Strouhal number for the two- and three-dimensional flows is about the same.

Flow-induced vibration for an array of cylinders has relatively limited number of studies compared with previous mentioned configurations. The investigation for VIV of multiple cylinders started with one flexible cylinder surrounded by rigid cylinders and later carried on to a stage that every cylinder is flexible. Price *et al.* [67] carried out experiments for a staggered array of several rows of rigid cylinders in air with one of them replaced by a flexible cylinder. They discovered that Strouhal numbers  $S$  did not change from one row to another, and  $S$  tended to increase as  $Re$  increases. Kevlahan [68] found that if a single cylinder with 1DOF in the transverse direction is surrounded by fixed cylinders (a common experimental configuration), the flow asymmetries caused by the movement of the central cylinder relative to its neighbours generates a "galloping" type instability in addition to the pure vortex-induced vibration of the isolated cylinder case. Kevlahan [68] also argued that the negative damping theory [69] was inconsistent with the Navier-Stokes simulation results. Also, 1DOF configuration of the tube caused great overestimation of the critical velocity, while Navier-Stokes simulations which allow all tubes to move in 2DOF give results in good agreement with experiment. VIV of multiple cylinders with each of them having 1DOF was simulated numerically by Zhao *et al.* [63]. They found that the vibration of the cylinders spread downstream with the increase of reduced velocity (see Figure 2.12). The vibration amplitudes of the downstream cylinders peaked at higher reduced velocities than that of a single cylinder. The maximum possible response amplitudes occurred at the most downstream cylinders.

To summarise this section, most common configurations of multiple cylinders were the 4 cylinders in square arrangement (most often also inline), and circular arrays with more than 7 cylinders. All cases in the literature were subjected to steady flow, and the focus of the study was on the flow patterns. In other words, similar to studies for two cylinders, quantitative relationship between configurations (i.e. input) and results (i.e. output) for the cylinder arrays was not as well established as that for a single cylinder (see Section 2.1), which was possibly due to a limited number of experiments (or simulations) and the complexity caused by the increase of the cylinder number. Also, as 2DOF simulation achieves better agreement with experiment [68], further study can be carried out for cylinder array with 2DOF.

## 2.4 Summary

In summary of this chapter, although there have been numerous studies examining the VIV behaviour of elastically mounted cylinders and the flow patterns of stationary cylinders

exposed to moving fluid, the effect of a circular cylinder-VIV induced by the vibration of another cylinder in stationary fluid, rather than flowing fluid, has never been examined in detail. In this study, the situation is simplified to the interaction between two rigid cylinders immersed in stationary fluid, where one cylinder undergoes forced harmonic vibrations to disturb the fluid while the second cylinder responds to this disturbance with 1DOF. This research aims to achieve a clearer understanding on how a vibrating cylinder (possibly the flow-induced vibration) exerts its influence on a nearby cylinder in still water, excluding the effects led by a water flow. This research mainly focuses on the sensitivity of the system behaviour to the initial gap ratios between the two cylinders, as well as the oscillating amplitude and the frequency of the active cylinder, whereas the non-dimensional mass ratio of both cylinders is kept constant as 2.5 and the specified vibration is at a low Reynolds number of 100.

# Chapter 3

## Numerical Method

The physics of multi-cylinder interaction was simulated by a numerical model — an in-house FORTRAN code provided by Prof. Ming Zhao from Western Sydney University. The code uses the streamlined upwind Petrov-Galerkin finite element method (FEM) with arbitrary Lagrangian-Eulerian (ALE) method and solves the two-dimensional (2D) Navier-Stokes equations directly (DNS) to simulate the case presented in Section 4.1.

Therefore, this chapter introduces the governing equations (Section 3.1) of the numerical model, the implemented FEM (Section 3.2) and ALE (Section 3.3) algorithms, as well as three main stream turbulence modelling strategies (Section 3.4).

### 3.1 Governing Equations

The simulations were carried out by applying a non-commercial FORTRAN code obtained from Prof. Ming Zhao in Western Sydney University. The code's governing equations are the two-dimensional incompressible Navier-Stokes equations. The Arbitrary Lagrangian Eulerian (ALE) scheme was implemented to move the boundaries of the cylinder surface. In the ALE scheme, the motion of nodes on computational mesh was configured to be independent of the fluid velocity to avoid excessive mesh distortion. Here the velocity  $(u, v)$ , the time  $t$ , the coordinate  $(x, y)$ , and the pressure  $p$  are non-dimensionalised as  $(u, v) = (\tilde{u}, \tilde{v})/(f_n D)$ , and  $p = \tilde{p}/(\rho f_n^2 D^2)$ , where the dimensional parameters are noted by tilde,  $D$  is the diameter of a circular cylinder,  $f_n = \sqrt{k/m}/2\pi$  is the structural natural frequency of the system, and  $\rho$  is the fluid density. The non-dimensional incompressible NS equations with ALE method can thus be expressed as Equations (3.1) and (3.2):

$$\frac{\partial u_i}{\partial t} + (u_j - u_{j,mesh}) + \frac{\partial u_j}{\partial x_j} + \frac{\partial p}{\partial x_i} = \frac{V_r}{Re_m} \frac{\partial^2 u_i}{\partial x_j \partial x_j} \quad (3.1)$$

$$\frac{\partial u_i}{\partial x_i} = 0 \quad (3.2)$$

where  $x_1 = x$  and  $x_2 = y$  are the Cartesian coordinates;  $u_i$  is the fluid velocity component in the direction of  $x_i$ ;  $u_{j, mesh}$  is the velocity of corresponding moving mesh nodes;  $V_r = U / (f_n D)$  is the non-dimensional free stream velocity;  $Re_m = U_m D / \tilde{v}$  is Reynolds number. This non-dimensional method also results in cylinder's oscillation frequency non-dimensionalised as  $f = \tilde{f} / f_n$ .

In terms of cylinder's motion, the vibration of 1DOF elastically mounted cylinder is described as Equation (3.3):

$$\frac{\partial^2 y}{\partial t^2} + 4\pi\zeta \frac{\partial y}{\partial t} + 4\pi^2 y = \frac{2}{\pi} \frac{V_r^2 C_y}{m^*} \quad (3.3)$$

where  $y$  is the cylinder's displacement in  $y$  direction;  $\zeta = c / (2\sqrt{km}) = 0$  is the damping ratio with  $c$  and  $k$  being the damping constant and spring stiffness of the system, respectively; and  $C_y = F / 0.5\rho D U^2$  is the force coefficient in the  $y$  direction with  $F$  being the hydrodynamic force on the cylinder in the  $y$  direction.

## 3.2 Finite Element Method

As my research was carried out with the code implementing finite element method (FEM), I present in this section a brief description and explanation of it.

FEM is commonly introduced as a special case of Galerkin methods [70], which are a class of numerical analysis methods for converting a continuous operator problem (e.g. a differential equation) into a discrete problem. The application of Galerkin methods is principally equal to applying the variational method of parameters to a function space by transforming the equation into a weak formulation. Typically some constraints are then applied to the function space to characterize the space with a finite set of basis functions. [71]

The finite element method (FEM) is defined as a numerical technique for finding approximate solutions to boundary value problems for partial differential equations [72]. To be exact, it is "a general discretisation procedure of continuum mechanics problems posed by mathematically defined statements" [73]. The term "finite element" was born as a engineering analogy, and seemingly firstly used by Clough [74]. FEM is also referred to as finite element analysis (FEA).

Generally speaking, the process of FEM consists of two steps. First, a large computational domain is divided into a collection of sub-domains (finite elements). Second, the simple

equations that model these finite elements are then recombined into a large system of equations that models the entire problem, which is subsequently calculated from the initial values of the original problem to obtain a numerical answer. [70]

In the first step, the element equations are simple equations that locally approximate the original complex equations, which is often partial differential equations (PDE). This approximation process integrates the inner product of the residual and the weight functions and set the integral to zero. In other words, it is the minimisation of the approximation error by fitting trial functions into the PDE. The residual is the error caused by the trial functions, and the weight functions are polynomial approximation functions that project the residual. This process eliminates all the spatial derivatives from the PDE, thus approximating the PDE locally with a set of algebraic equations for steady state problems and a set of ordinary differential equations for transient problems. These equation sets are the element equations. They are linear if the underlying PDE is linear, and vice versa. Algebraic equation sets that emerge in the steady state problems are solved using numerical linear algebra methods, while ordinary differential equation sets that arise in the transient problems are solved by numerical integration using standard techniques such as Euler's method or the Runge-Kutta method. [70]

In the second step, a global system of equations is generated from the element equations through a transformation from the sub-domains' local nodes' coordinates to the domain's global nodes' coordinates. Appropriate orientation adjustments are also included in the spatial transformation. This process is often carried out by FEM software using coordinate data generated from the sub-domains. [70]

The popularity and fame of FEM should be attributed to its various advantages. First and foremost, FEM can accurately represent very complex geometry and can include dissimilar material properties, which enables FEM to deal with a wide range of engineering problems, for example, solid mechanics, fluid dynamics, heat transfer and electrostatic problems. FEM can also handle complex restraints and complex loading (e.g. nodal load, element load and time or frequency dependent loading) [75]. On the other hand, FEM also has its disadvantages. Different from analytical solutions, FEM obtains only approximate solutions, which means FEM has inherent error and does not allow the examination of system response to changes in various parameters. In addition, mistakes by users without full understanding of FEM is serious, because incorrect input will result in useless output [76, 77].

In addition, as for FEM application in fluid mechanics, much of the earlier activity to solve fluid mechanics problems applied a "finite difference" formulation and later a derivative of this as the "finite volume" technique. Competition between FEM and finite difference technique has led to a much slower adoption of FEM in fluid mechanics than in structures.

However, there are many advantages of using the FEM, which not only allows a fully unstructured and arbitrary domain but also provides an approximation which in self-adjoint problems is superior or at least equal to that provided by finite differences. [78]

### 3.3 Arbitrary Lagrangian-Eulerian Method

In the algorithms of continuum mechanics, the Lagrangian description and the Eulerian description are two most classical descriptions. In Lagrangian algorithms, each individual node of the computational mesh follows the associated material particle during motion, while in Eulerian algorithms, the computational mesh is fixed and the continuum moves with respect to the grid. The arbitrary Lagrangian-Eulerian (ALE) description was developed for combining the advantages of these classical descriptions. Meanwhile, it alleviates their drawbacks as far as possible. Moreover, the robustness and efficiency of ALE algorithm can be further improved by integrating other existing techniques (e.g. adaptive mesh, local remeshing and parallel computing). [79, 80]

The ALE algorithm allows the computational mesh inside the domains to move arbitrarily to optimize the shapes of elements, while the mesh on the boundaries and interfaces of the domains can move along with materials to precisely track the boundaries and interfaces of a multi-material system. Also, ALE formulations can be reduced to either Lagrangian formulations by equating mesh motion to material motion or Eulerian formulations by fixing mesh in space. As a result, the versatility of ALE method allows it to perform comprehensive engineering simulations, including heat transfer, fluid flow, fluid-structure interactions and metal-manufacturing.

### 3.4 Turbulence Modelling Strategies

The current research is using two-dimensional (2D) direct numerical simulation (DNS). In other words, the Navier-Stokes equations are solved directly by the code without a turbulence model. The application of 2D-DNS is justified by the simple geometry (two cylinders) and a low Reynolds number  $Re_m = 100$ . Nevertheless, future researches may investigate the influence of turbulence on the simulation results, especially on high Reynolds numbers. Therefore, here I present an introduction to the turbulence phenomenon, as well as three main categories of turbulence modelling strategies.

Turbulence is a commonly observed phenomenon in many engineering applications (e.g. fluid flow with high  $Re$  [81]). Turbulence is always three-dimensional (3D) and unsteady with a large range of scale motions [82]. What is more, the instantaneous range of scales in

turbulent flows surges with the Reynolds number [83]. Exact physical nature of turbulence has not been fully understood, yet it can be modelled to a sufficient degree of accuracy in numerical simulations [82]. A main issue with numerical simulation (as well as measurement) of turbulence is the vast range of scales that must be resolved. To deal with it, the applied computational domain size must be at least in an order of magnitude larger than the scales characterising the turbulence energy, while the computational mesh must be dense enough to resolve the smallest dynamically significant length-scale (the Kolmogorov micro-scale [84]) for accurate simulation [82].

In CFD, turbulent flow simulation strategies can be divided into three categories: Direct Numerical Simulation (DNS), Large Eddy Simulations (LES), and Reynolds Averaged Navier-Stokes Simulations (RANS). DNS numerically solves the full unsteady Navier-Stokes equations, and is the most accurate method of solving turbulence in fluids [85, 86]. DNS provides complete knowledge, unaffected by approximations, at all points and times considered. However, it has two major drawbacks - its extreme computational cost, and severe limitation on the maximum Reynolds number that can be considered, which means it is more of a research tool rather than for industrial applications [87]. LES only resolves the large scales of motion, and models the small scales of motion, via a low-pass filtering of the Navier-Stokes equations. Compared with DNS, the computational cost of LES is reduced, yet the small-scale information is also lost [88, 89]. RANS extracts the time-averaged quantities of fluid motion, discarding the fluctuating quantities. For most of the industrial applications, RANS can provide the required accuracy, and is less demanding for computational resources compared with LES. Nevertheless, RANS models' accuracy does not improve with the mesh resolution when the fineness of mesh goes beyond a certain level [90, 85].

### 3.4.1 Direct numerical simulation

The irregular and random behaviour of turbulence can be represented by a fairly simple set of equations – the Navier-Stokes equations. What is more, there is no analytical solutions to turbulent flows. Therefore, a complete description of a turbulent flow, where the flow variables (e.g. velocity and pressure) are a function of space and time, can only be achieved by numerical solutions of the Navier-Stokes equations. These numerical solutions are then termed as "direct numerical simulations" (DNS). [83]

In terms of the mesh density requirement, the Kolmogorov length scale,  $\eta = (\tilde{v}^3/\varepsilon)^{1/4}$ , has been a common standard for the smallest scale that requires resolving, where  $\varepsilon$  is the average dissipation rate of turbulence kinetic energy per unit mass, and  $\tilde{v}$  is the fluid kinematic viscosity [84]. Nevertheless, this requirement may be conservative. The smallest resolved length-scale is required to be of  $O(\eta)$ , not equal to  $\eta$  [83]. For example, Moser &

Moin [91] found that most of the dissipation in the curved channel occurs at scales greater than  $15\eta$  (based on average dissipation).

DNS is a useful tool for turbulence studies. Significant insight into turbulence physics has been gained from DNS of certain idealised flows that cannot be easily attained in the laboratory. [83]

### 3.4.2 Large eddy simulation

Large Eddy Simulation (LES) is a turbulence modelling strategy that falls between RANS and DNS in terms of computational time and simulation accuracy. The core idea of LES is to cut the computational cost by avoiding the smallest length scales of the turbulent flow simulation, i.e. the most computationally consuming part, through low-pass filter of the Navier-Stokes equations [88]. A low-pass filter passes signals with a frequency lower than a certain cut-off frequency and attenuates signals with frequencies higher than the cut-off frequency [92], which can be viewed as a time- and spatial-averaging. The low-pass filter removes small-scale information from the numerical solution. However, the unresolved small-scale turbulent effect on the flow field must be modelled, as the filtered small-scale information is necessary for problems sensitive to small-scale turbulence [88], such as near-wall flows [93, 94], reacting flows [95], and multiphase flows [96].

LES came out first in 1963 by Smagorinsky [97]. For LES applications in early days, it was applied to flow problems with simple geometry and low Reynolds numbers, such as homogeneous turbulence, mixing layers, plane channel flows. Now focus of LES researches has shifted to more complex configurations where the RANS approach has failed. Nevertheless LES has not replaced RANS models and cannot replace it for the near future to become the main computational analysis tool for practical engineering problems. That is because of two main reasons: firstly, although computing power has developed rapidly for decades, it is still overly consuming to perform LES for practical engineering flow problems. Secondly, LES is still not mature enough, so users without sufficient knowledge can hardly achieve outputs with satisfying fidelity. For the foreseeable future LES will not become a design tool that can be employed by persons without extensive experience on LES techniques. [82]

In addition, despite the traditional LES method, there are also some related approaches such as ILES (Implicit LES) or called MILES (Monotone Integrated LES), VLES (Very LES) and the hybrid LES/RANS approach.

### 3.4.3 Reynolds-averaged Navier–Stokes simulation

Among various semi-empirical mathematical models, the k-omega model is a commonly used and extensively tested turbulence model. The model enables the closure of Reynolds-averaged Navier-Stokes (RANS) equations. As a two-equation model, k-omega model include two extra transport partial differential equations to represent the turbulent properties of the flow with two variables:  $k_t$  and  $\omega_t$ , where  $k_t$  is the turbulence kinetic energy while  $\omega_t$  is the specific rate of dissipation from turbulence kinetic energy  $k_t$  into internal thermal energy.  $k_t$  stands for the energy in the turbulence, while  $\omega_t$  stands for the scale of the turbulence. [98, 99]

As a hybrid model combining the k-omega and the k-epsilon models, SST k-omega model is one of the most validated models. The shear stress transport (SST) formulation brings together the best of k-omega and k-epsilon. A blending function is used to activate the Wilcox model near the wall and the k-epsilon model in the free stream, which makes the model applicable all the way down to the wall through the viscous sub-layer. The SST k-omega model can therefore be used as a Low-Re turbulence model without any extra damping functions. In addition, the k-epsilon model is activated in the free-stream condition in order to avoid the k-omega model's over-sensitivity to the inlet free-stream turbulence properties. SST k-omega model is often credited for its good behaviour in adverse pressure gradients and separating flow, as well as the accuracy for solving flow near wall. On the other hand, the SST k-omega model produces excessively large turbulence levels in regions with large normal strain (e.g. stagnation regions and regions with strong acceleration), which is less profound in a k-epsilon model. Also, the SST model sometimes has slow convergence, as a result, the initial conditions are often achieved by k-epsilon or k-omega models. [100, 101]



# Chapter 4

## Numerical Results

The numerical model described in Chapter 3 was applied to simulate a simplified case of two interacting cylinders in still water (Figure 4.1). The dimensional analysis (Section 4.2) was exploited to reduce the parameters in need of consideration. After that, I carried out mesh independence study (Section 4.3) and validation (Section 4.4) to ensure the coherence between the model and the reality. At last, cylinder-interaction results (Section 4.5) were produced, and found several interesting conclusions (Section 4.7).

### 4.1 Case Setup

The geometry of case setup is demonstrated in Figure 4.1. Two identical cylinders separated by distance  $G$  are immersed in still fluid. Cylinder 1 (C1) vibrates in simple harmonic motion, which is described as  $Y_1 = A_1 \sin(2\pi f_1 t)$ . Cylinder 2 (C2) is mounted to a spring, and has only 1-Degree-Of-Freedom (1DOF) along the y-axis.

### 4.2 Dimensional Analysis

Dimensional analysis is a mathematical method used to predict physical parameters that influence the flow in fluid mechanics, heat transfer in thermodynamics, and so forth. The analysis involves the fundamental units of dimensions [M], [L] and [T] (i.e. mass, length, and time). It is helpful in experimental studies as it offers a guide to factors that significantly affect the studied phenomena. [102]

For the case studied in this research (see Figure 4.1), Buckingham theorem is applied to find out the dimensionless groups influencing the simulation results. The procedure is as follows:

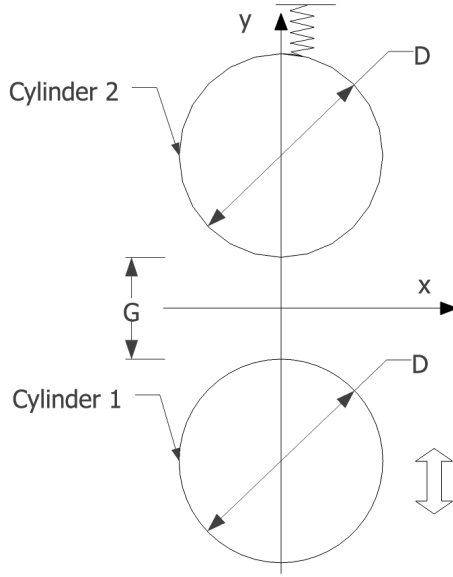


Fig. 4.1 Interaction between two cylinders: Cylinder 1 (C1) undergoes harmonic forced vibration while Cylinder 2 (C2) responds with 1DOF along y-axis with restoring force.

By my experience on the topic, for this case, there are 9 quantities and 3 dimensions:

$$\begin{bmatrix} D & f_n & m & \tilde{A}_1 & \tilde{f}_1 & \tilde{G} & \rho & \tilde{v} & \tilde{A}_2 \\ 0 & 0 & 1 & 0 & 0 & 0 & 1 & 0 & 0 \\ 1 & 0 & 0 & 1 & 0 & 1 & -2 & 2 & 1 \\ 0 & -1 & 0 & 0 & -1 & 0 & 0 & -1 & 0 \end{bmatrix} \begin{matrix} M \\ L \\ T \end{matrix}$$

where  $D$  is diameter of cylinder;  $f_{n2} = \sqrt{k/m}/2\pi$ , structural natural frequency of C2 (Cylinder 2);  $m$ , mass of C2;  $U_{m1} = 2\pi\tilde{A}_1\tilde{f}_1$ , maximum velocity of C1 (Cylinder 1);  $\tilde{f}_1$ , vibration frequency of C1;  $\tilde{G}$ , distance between C1 and C2;  $\rho$ , density of fluid;  $\tilde{v}$ , kinematic viscosity.  $A_2$ , vibration amplitude of C2, is the variable I am interested in.

According to Buckingham theorem, these quantities can be reduced to  $9 - 3 = 6$  independent dimensionless groups.

If  $D$ ,  $f_n$ , and  $m$  are selected as repeating variables, the 6 groups can be written as follows:

$$\pi_1 = \frac{\tilde{A}_1}{D}, \quad \pi_2 = \frac{\tilde{f}_1}{f_{n2}}, \quad \pi_3 = \frac{\tilde{G}}{D}, \quad \pi_4 = \frac{\rho}{mD^{-2}} = \frac{4}{\pi m^*}, \quad \pi_5 = \frac{\tilde{v}}{f_n D^2} = \frac{2\pi A_1 f_1}{Re_m}, \quad \pi_6 = \frac{\tilde{A}_2}{D}.$$

In other words,  $A_2$  can be determined by 5 independent dimensionless groups:  $A_1$ ,  $f_1$ ,  $G$ ,  $m^*$ ,  $Re_m$ , as seen in Equation (4.1):

$$\frac{\tilde{A}_2}{D} = f\left(\frac{\tilde{A}_1}{D}, \frac{\tilde{f}_1}{f_{n2}}, \frac{\tilde{G}}{D}, m^*, Re_m\right) \quad (4.1)$$

Table 4.1 Non-dimensional groups to determine a case

Mass ratio	$m^*$	$\frac{m}{\rho D^2 \pi / 4}$
Gap ratio	$G$	$\frac{\tilde{G}}{D}$
Amplitude ratio of C1	$A_1$	$\frac{\tilde{A}_1}{D}$
Frequency ratio of C1	$f_1$	$\frac{\tilde{f}_1}{f_n}$
Reynolds number regarding $U_{1m}$	$Re_m$	$\frac{2\pi\tilde{A}_1\tilde{f}_1D}{v}$

### 4.3 Mesh Independence Study

The computational domain was divided into quadrilateral 4-node finite elements; the mesh for the validation case to be discussed is shown in Figure 4.4. It has a square non-dimensional computational domain with length & width of 60 times the diameter, thus the ratio of the cylinder diameter to the computational domain width is 1.67%. The mesh for a configuration with two cylinders with gap ratio  $G = 0.2$  is shown in figures Figure 4.2, which has a square non-dimensional computational domain with length and width both equal to 160. Separate meshes were generated for situations with different initial gap ratios (see Table 4.2). For the current simulations, the non-dimensional time steps were chosen as  $\Delta t = 0.002D/U_{1m} = 0.002/(2\pi A_1 f_1)$ . The non-dimensional viscosity was calculated as  $v = 2\pi f_1 A_1 / Re_m$ .

For Courant number on the radial direction, in the boundary layer near the cylinder boundary, the fluid velocity (relative to the cylinder velocity) is almost parallel to the solid surface. Therefore, the velocity in the radial direction near the cylinder surface is very small, leading to a small Courant number on the radial direction  $C_r < 1$ . For Courant number on the circumferential direction, the number of finite elements on the circumference of the cylinder ranges from 134 to 876 (see Table 4.2), which means the non-dimensional element size along the circumferential direction is  $\Delta s = 0.004 \sim 0.023$ . As a result, the Courant number on the circumferential direction is  $C_s = 0.002/\Delta s \approx 0.085 \sim 0.558 < 1$ .

To ensure that the meshes are dense enough to produce accurate results, a mesh dependency study was conducted. The case of  $G = 0.2$ ,  $A_1 = 0.1$ ,  $f_1 = 0.825$  was selected for the study, because the vibration in this case has the greatest  $A_2/A_1$ . A series of meshes with various  $N_c$  (i.e. element number along each cylinder surface) and  $\Delta r_{min}$  (i.e. minimum non-dimensional element size on the radial direction of the mesh) was simulated for this case.

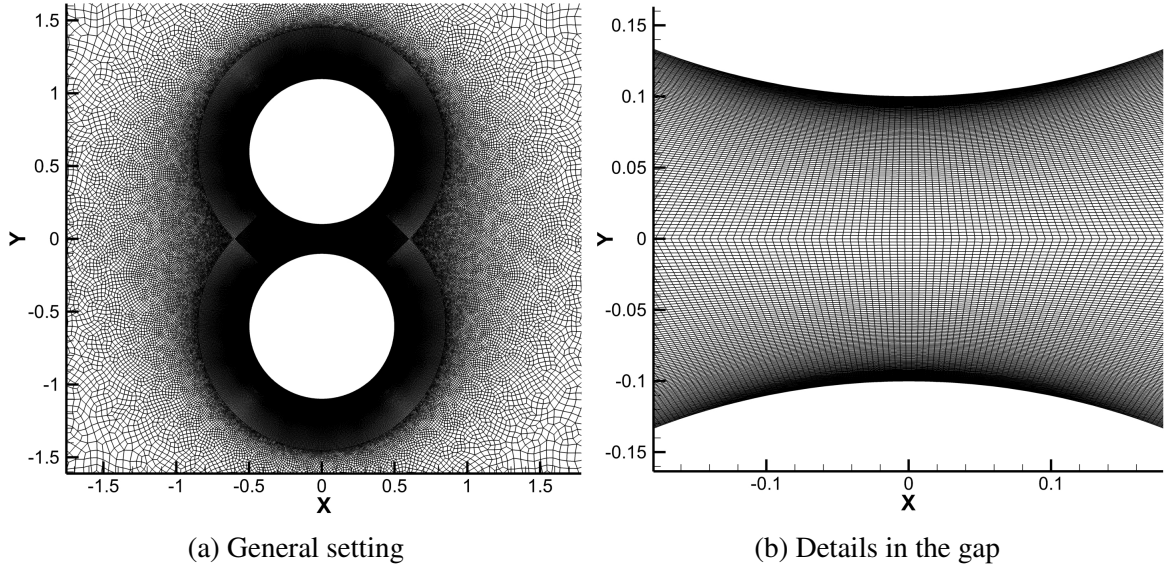


Fig. 4.2 Computational mesh for two cylinders with  $G=0.2$ .

The frequency of C2 remained constant ( $f_2 = f_1 = 0.825$ ) with the variation of  $N_c$  &  $\Delta r$ , yet the amplitude of C2 slightly changed, as seen in Figure 4.3a. It can be seen in Figure 4.3 that, at  $\Delta r_{min} = 0.000902$  &  $116 \leq N_c \leq 266$ ,  $A_2$  slightly varies by 0.113% and converges at  $N_c \geq 266$ . Figure 4.3b shows that  $A_2$  converges with the decrease of  $\Delta r_{min}$  and varies for a mere 3%, at  $N_c = 296$  &  $0.00105 \leq \Delta r_{min} \leq 0.0045$ . For all the applied meshes (see Table 4.2),  $\Delta r_{min}$  was less than 0.0045 and the  $N_c$  was larger than 144. In other words, the applied meshes are dense enough for the simulations.

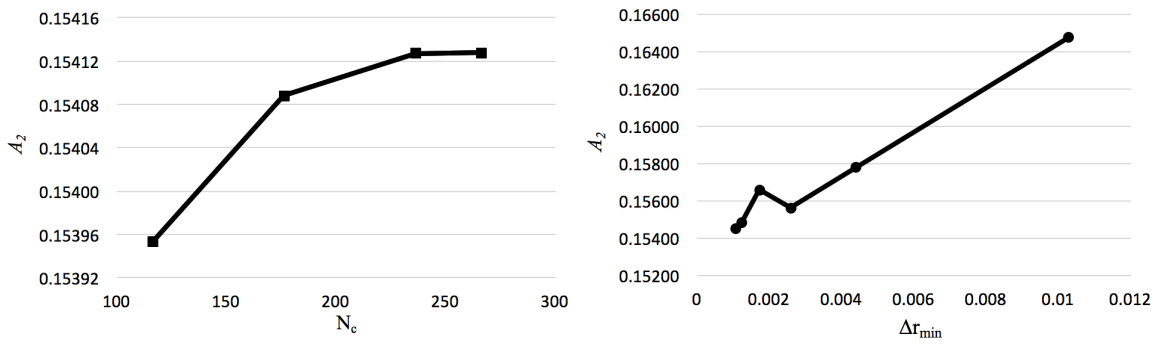


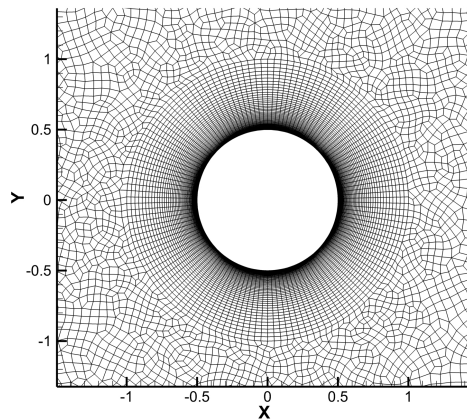
Fig. 4.3 The results of the mesh dependency study.

Table 4.2 Computational meshes for various gap ratios

G	Total nodes	Nodes along two cylinders	Nodes along each cylinder	Length of square boundary
Single	55 159	N/A	134	60
3.00	136 711	384	192	160
1.25	129 295	384	192	160
1.00	127 791	288	144	160
0.50	178 437	952	476	160
0.40	170 129	952	476	160
0.30	180 299	952	476	160
0.20	242 329	1752	876	160
0.10	183 599	952	476	160
0.05	131 746	952	476	160

## 4.4 Validation

The validation case was set to be a single cylinder (see Figure 4.4 and Table 4.2) oscillating harmonically in still fluid at  $KC = U_{max}/(fD) = 5$ ,  $Re_m = U_mD/\nu = 100$ . The simulation results were compared with the experimental data obtained by Dutsch [103], as seen in Figure 4.5. The horizontal & vertical velocity components ( $u$  &  $v$ ) of the predicted and measured data are compared along  $y/D = 0.6, 0, -0.6$  and  $-1.2$  for phases  $\psi = 180^\circ, 210^\circ, 330^\circ$ . In Figure 4.5, the lines represent the simulation results, while symbols stand for experimental data. It can be seen that the simulation results match with the experimental data well. In addition, the applied numerical model has been validated in several VIV-studies [6, 104–106].

Fig. 4.4 Single cylinder mesh for validation case with  $N_c = 134$  and  $\Delta r \approx 0.00183$

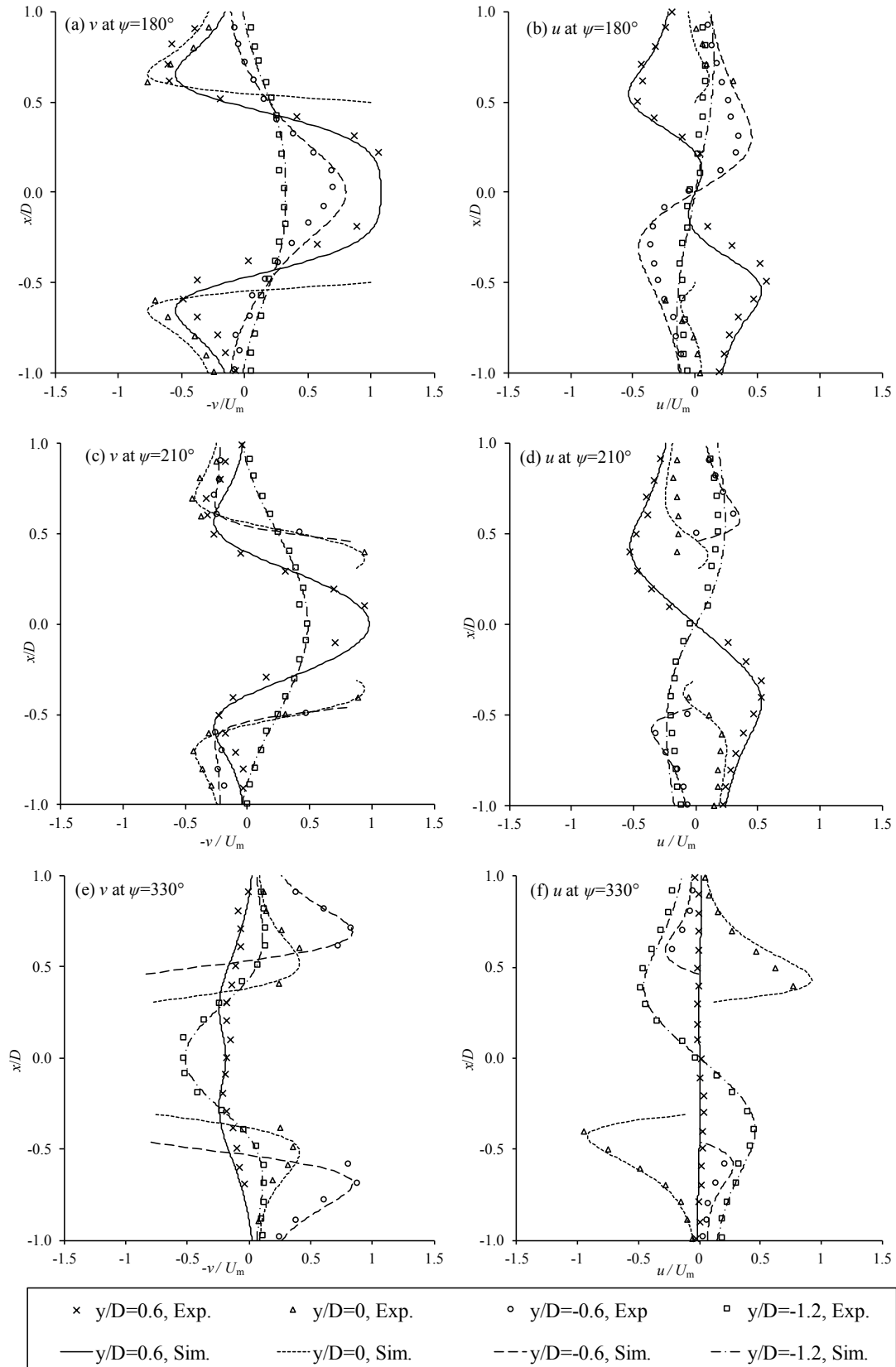


Fig. 4.5 Comparison of fluid velocity distribution between the numerical simulation results and the experimental data by Dutsch [103]

## 4.5 Cylinder-interaction Results

As Cylinder 1 (C1) experiences forced vibration, the surrounding fluid is disturbed, generating vortices around C1. The disturbed fluid induces the vibration of Cylinder 2 (C2), which also generates its own vortices. The vortices adjacent to C1 and C2 interact with one another, lending extra complication to the situation.

The interaction between C1 and C2 was simulated with a series of initial gap ratios G, such that  $G = 0.025 \sim 3$ . C1's forced vibrational amplitude was configured to be smaller than the corresponding gap ratio to avoid collision between cylinders, and C1's non-dimensional frequency ranges from 0.05 to 2.4.

For all the cases simulated, the frequency of C2 was identical to C1 ( $f_1 = f_2$ ), as seen in Figure 4.6. In addition, it is interesting that, as  $f_1$  increased from 0.05 to 2.5, the motion of C1 and C2 gradually changed from being in anti-phase (see Figure 4.6a) to being in phase (see Figure 4.6f), and  $A_2$  reaches maximum when  $f_1$  is slightly less than the critical value (around 0.8) between in anti-phase and in phase. After  $A_2$  reaches maximum, the motion of C1 and C2 remains in phase (see Figures 4.6e and 4.6f).

Figure 4.7a shows the relationship between C2's response amplitude ( $A_2$ ) and the C1's frequency  $f_1$ . Generally speaking, C2's response amplitude in Figure 4.7a ranges from almost 0 to 0.22. There are two peaks: a smaller one at  $0.4f_n$  and a greater one at  $0.8f_n$ . For the same  $f_1$ , cases with greater  $A_1$  always have greater  $A_2$ . As  $f_1$  increases beyond 1.6,  $A_2$  does not change significantly.

Figure 4.7b demonstrates the amplification of the vibration, with the y-axis representing  $A_2/A_1$ . For the peak at  $f_n = 0.4$ , the pattern is similar to Figure 4.7a. However, the major peak at  $f_n = 0.8$  has a pattern that is different from Figure 4.7a. The case with  $A_1 = 0.5$  has the largest value of  $A_2/A_1$  being 0.104; the cases with  $A_1 = 1 \& 2.5$  have the peak value of  $A_2/A_1$  being 0.085; when  $A_1 = 1.5$  and 2.0, the peak  $A_2/A_1$  are 0.078 and 0.075, respectively. The rise of  $A_1$  causes the decrease of  $(A_2/A_1)_{peak}$  until  $A_1 = 1.5$ , after which the change in  $(A_2/A_1)_{peak}$  is small.

Figure 4.8 demonstrates the variation of  $A_2/A_1$  with  $f_1$  when  $G = 0.2, 1.0, 1.25$  and  $A_1 = 0.025 \sim 1$ . On the whole, for the cases simulated, C2's relative response amplitude  $A_2/A_1$  in Figure 4.8 varies from 0 to 2. Similar to Figure 4.7b, there is one large peak around  $f_1 = 0.8$  accompanied by a small peak at  $f_1 = 0.4$ . The values of  $A_2/A_1$  for  $G = 0.2$  are generally larger than those for  $G = 1, 1.25$ , and the patterns of lines for  $G = 0.2, 1$  and 1.25 are very similar. For  $G = 0.2, 1$  and 1.25,  $A_1$  and  $(A_2/A_1)_{peak}$  are inversely related. Moreover,  $A_1$  is also inversely related to the resonance frequency, i.e. the  $f_1$  corresponding to  $(A_2/A_1)_{peak}$ . As  $f_1$  increases above 1.0,  $A_2/A_1$  gradually drops.

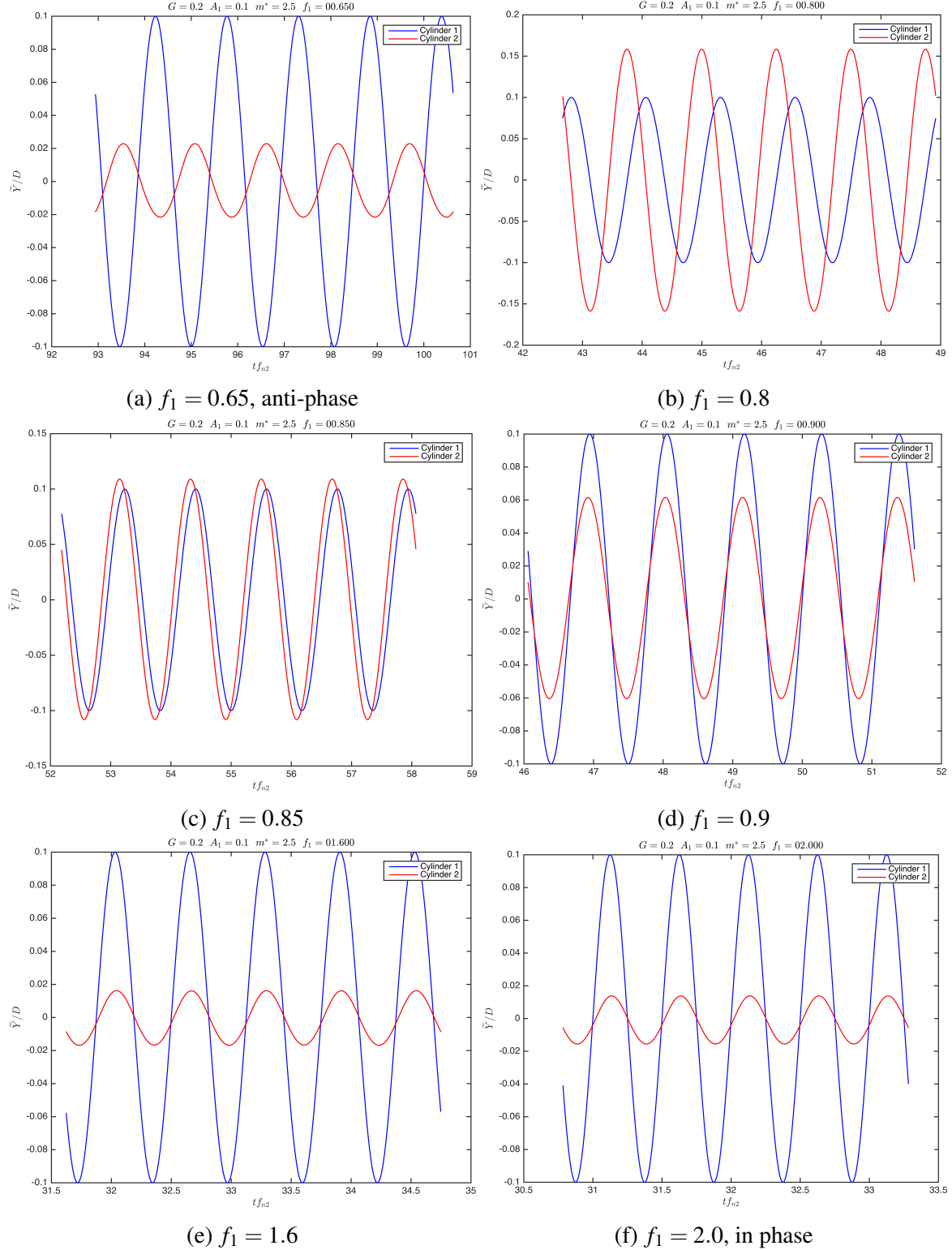


Fig. 4.6 Comparison between Cylinder 1 and Cylinder 2's displacement histories at  $G = 0.2$ ,  $A_1 = 0.1$ ,  $f_1 = 0.65, 0.8, 0.85, 0.9, 1.6, 2.0$ . The blue line denotes Cylinder 1, while red line denotes Cylinder 2.

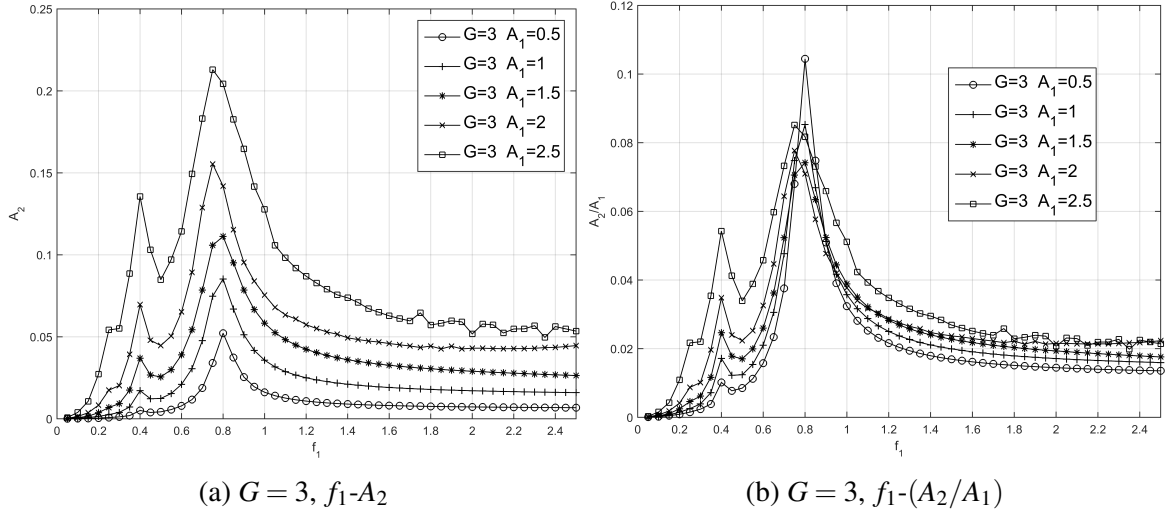


Fig. 4.7 (a) Variation of C2's response amplitude with the frequency of C1 for  $G = 3, A_1 = 0.5, 1.0, 1.5, 2.0, 2.5$ , and (b) Variation of C2's amplification factor with the frequency of C1, for  $G = 3, A_1 = 0.5, 1.0, 1.5, 2.0, 2.5$ .

In Figures 4.7 and 4.8, the maximum values of  $A_2/A_1$  are always found to occur at around  $f_1=0.8$ , rather than  $f_1=1$ , which is because at low mass ratios the natural frequency of the structural in the fluid is less than the structural natural frequency [6]. The increase of  $A_1$  leads to the reduction of the peak value of  $A_2/A_1$  and the decrease in the resonance frequency.

In terms of amplitude amplification, Figures 4.8e and 4.8f demonstrates the change in C2's amplitude ( $A_2/A_1$ ) with the frequency of C1, with  $G = 0.2$  and  $A_1 = 0.05, 0.1$ . It is notable that the value of  $A_2/A_1$  goes beyond 1.0 at  $f_1 = 0.8$ , meaning the consequent amplitude of C2 is greater than the input amplitude of C1. Moreover, Figure 4.9 shows the variation of peak values for  $A_2/A_1$  with respect to  $G$ . It can be seen that  $A_2/A_1$  is above 1.0 when  $G \leq 0.4$ , and stays almost constant when  $G \leq 0.2$ .

In addition, the shift of vibration centre was observed in the cases with  $G = 3$ . Sometimes, the displacement of the vibration centre was even larger than the amplitude of the vibration. When  $G = 3, A_1 = 1.0 \sim 2.5$  with increment of 0.5, and  $f_1 = 0.05 \sim 2.5$  with increment of 0.05, the contour in Figure 4.11 shows combination of  $f_1$  and  $A_1$  for vibration centre displacement  $\Delta Y = A_2$ . For the area above the red line (i.e. large  $f_1$  and  $A_1$ ), the vibration centre displacement becomes greater than the induced vibration amplitude  $A_2$  and eventually exceeds 14 times of  $A_2$  for the combination of greatest  $A_1$  &  $f_1$ .

Some examples of vibration centre shift are shown in Figure 4.10. Figure 4.10a depicts examples of C2's displacement histories for  $G = 3.0, A_1 = 0.5, 1.0, 1.5, 2.0$ , and  $f_1 = 2.5$ . As the amplitude of C1 increases, the vibration centre of C2 keeps moving away from C1. A sudden drop of vibration centre from  $+0.4$  to  $-0.35$  occurs at  $5 \leq t f_n \leq 7$  and  $A_1 = 2.0$ . After

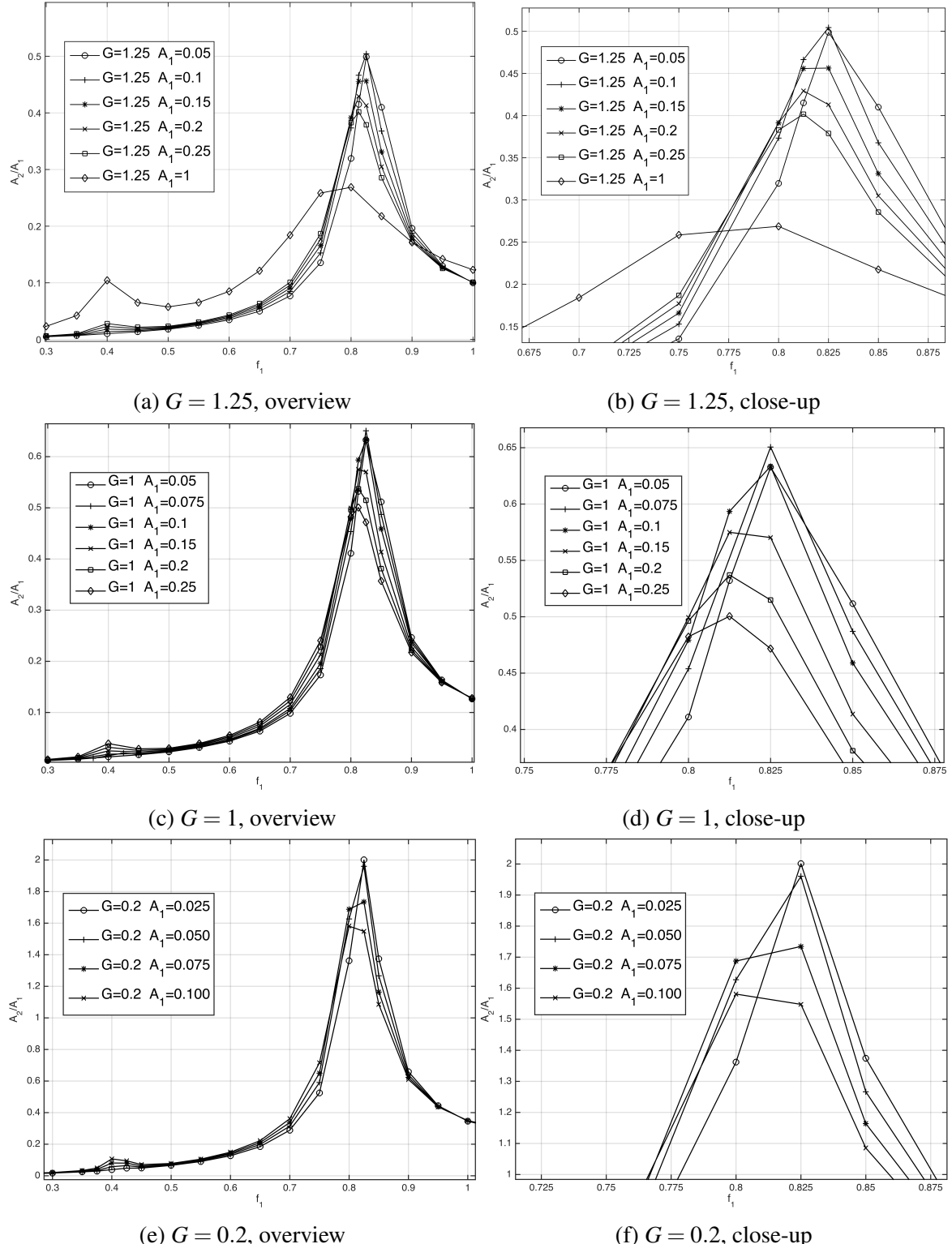


Fig. 4.8 (a) & (c) & (e) Variation of C2's amplification factor with the frequency of C1, for  $G = 0.2, 1, 1.25$ ;  $A_1 = 0.025, 0.05, 0.075, 0.1, 0.15, 0.2, 0.25, 1$ . (b) & (d) & (f) Close-up view near resonance.

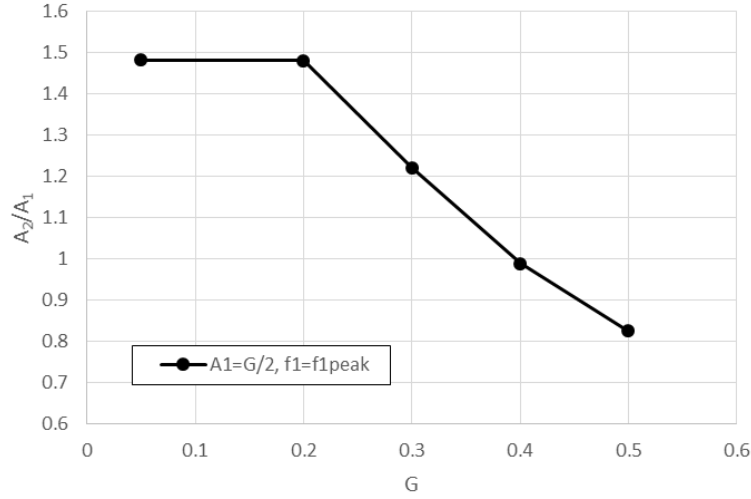


Fig. 4.9 Variation of maximum  $A_2/A_1$  with the gap ratio  $G$ , where the value of  $A_1$  is always  $G/2$ .

the sudden drop, the vibration centre of C2 remains steady at -0.35, which is closer to C1 than at the start of the simulation. Figure 4.10b shows examples of C2's displacement histories for  $G = 3.0$ ,  $A_1=2.0$ ,  $f_1=0.8, 2.0, 2.5$ . As frequency rises, the magnitude of C2's vibration centre shift becomes more apparent. While the vibration centre for  $f_1 = 0.8$  remains constant at about +0.05, an abrupt decrease occurs for  $f_1 = 2.0$  and 2.5. Although the vibration amplitude at  $f_1 = 2.0$  and 2.5 is smaller than that of  $f_1 = 0.8$ , the vibration centre shift at these larger frequencies are much greater than the vibration amplitude.

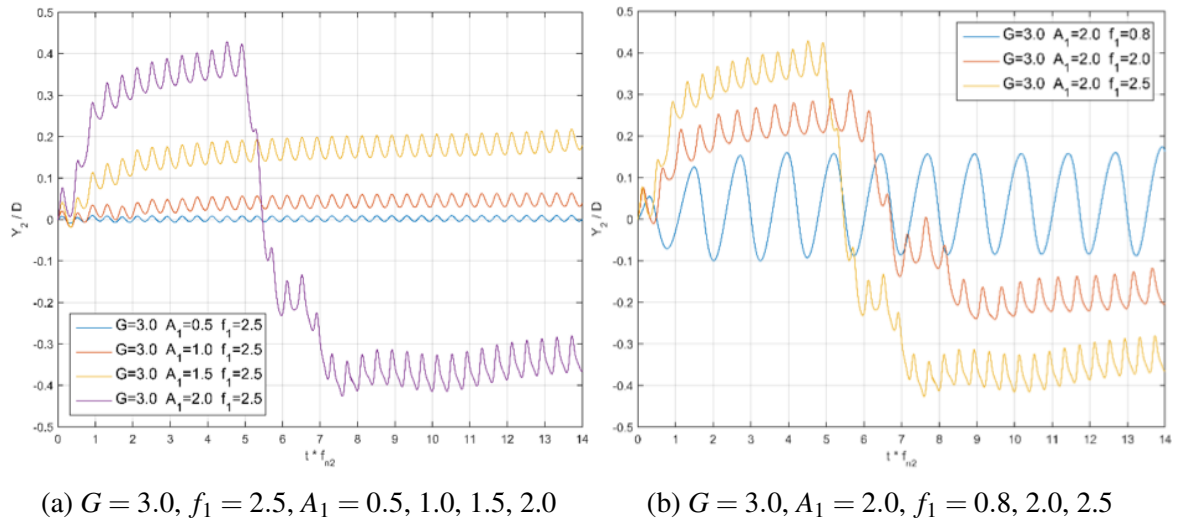


Fig. 4.10 Displacement time histories of C2

## 4.6 Discussion

For all the cases simulated (see Figure 4.8), major resonance occurs when  $\tilde{f}_1 = 0.8$ . That is because  $f_{wn}/f_n = \sqrt{m^*/(m^* + C_A)}$ . Also,  $C_A$  of a cylinder can be approximated as 1.273[107], which means  $f_{wn}/f_n = 0.814$ . This explains the large resonance peak at 80 percent structural natural frequency.

## 4.7 Summary

Using numerical simulations, we investigated the mechanical interactions between two submerged cylinders. The active cylinder C1 underwent forced vibration with specified amplitude and frequency. All the cases studied had constant Reynolds number of 100 and mass ratio of 2.5. The passive cylinder C2 responded to the oscillation of the active cylinder by way of the induced fluid motion in the following way:

1. The amplitude of C2 reached its maximum when the frequency of C1 was close to 80% of the C2's structural natural frequency ( $f_n$ ).
2. The increase of C1's amplitude led to the rise of C2's amplitude, but the decrease of the amplitude magnification factor ( $A_2/A_1$ ) and the slight decrease of the resonance frequency.
3. The vibration centre of C2 shifted away from the initial location for cases with  $\tilde{G}/D = 3$ , and the shift became increasingly obvious with the increase of  $A_1$  and  $f_1$ .
4. For cases with  $A_1 = G/2$ , the values of maximum  $A_2/A_1$  were above 1.0, at  $G < 0.4$ .

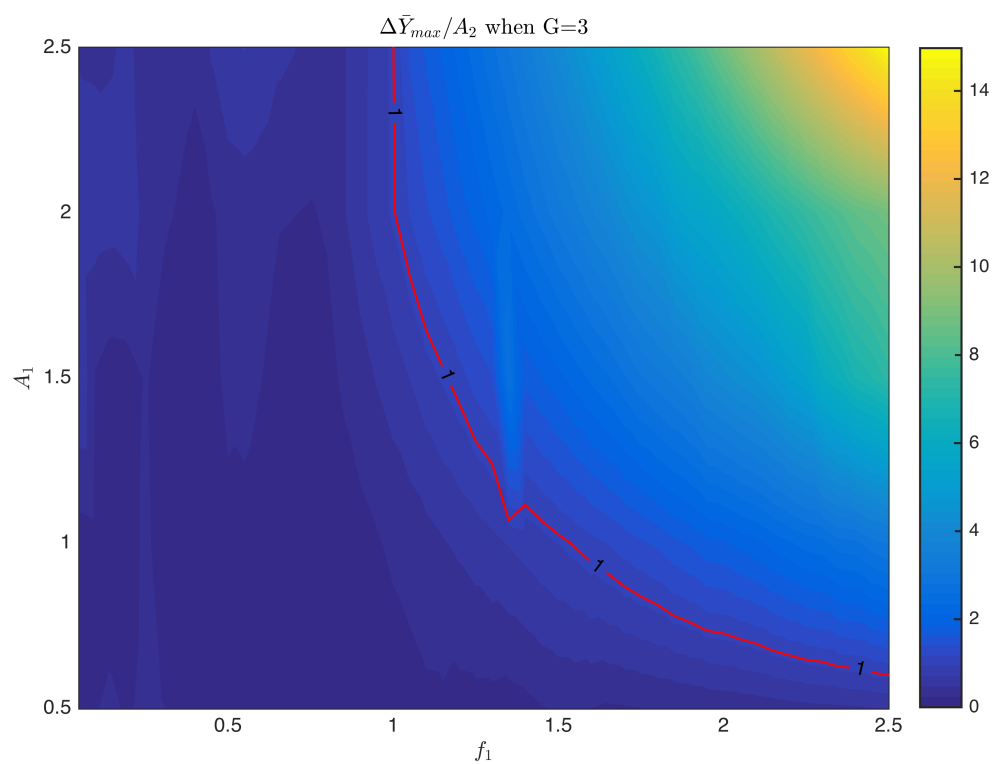


Fig. 4.11 Dependence of  $\Delta\bar{Y}/A_2$  on  $A_1$  &  $f_1$  for  $G=3$



# Chapter 5

## Conclusion & Future Plan

This chapter summarises the content of the entire report and plans the research work in the future.

### 5.1 Conclusion

This Ph.D. project reviews the dynamic characteristics of an elastically mounted cylinder in detail, and various research about multiple stationary or elastically mounted cylinders. Both experimental and numerical studies were addressed. The tendency is that more and more researches are carried out by numerical simulations rather than experiments. It can be seen that, despite applications in many fields including offshore and civil engineering, the dynamics of multiple cylinders exposed to a steady flow is still not fully understood. This research investigates the interaction between two cylinders in still water, which aims to simplify the case by excluding the influence from fluid flow. The current research implements the finite element method with arbitrary Lagrangian-Eulerian (ALE) method to solve the two-dimensional (2D) Navier-Stokes equations directly. The turbulence model was not included (i.e. it is DNS), because all current simulations had a low Reynolds number  $Re = 100$ . However, to accommodate situations with higher Reynolds numbers, the future simulation may apply the SST k-omega model (i.e. a RANS model) or LES genre models. The code was used to simulate the simplified case (see Figure 4.2a) with five determining non-dimensional groups (see Table 4.1). Simulation results demonstrated that resonance occurred at around  $f_1 = 0.8f_n$ , and the increase of C1's amplitude  $A_1$  raised C2's amplitude  $A_2$  yet decreased the amplitude magnification factor ( $A_2/A_1$ ). Vibration centre shift occurred at  $G = 3$  and became increasingly obvious with the increase of  $A_1$  and  $f_1$ .

## 5.2 Future Plan

In terms of my future work, more simulation cases with different gap ratios and C1's amplitude will be carried out, and further study will focus on cases with  $0.01 \leq G \leq 0.1$ . The Reynolds number will also be increased to explore cases with complicated flow regimes [108]. In order to conduct simulations with high Reynolds numbers, 3 dimensional numerical model and RANS turbulence model will be employed. Various mass ratios will be tested to explore their effects on the cylinder interaction results. Compressible Navier-Stokes equations may be applied for investigation on high mass ratio conditions (e.g.  $m^* = 250$  in air). Also, another case setup with transverse cylinder motion will be further investigated. This transverse setup is currently difficult, as the mesh is so distorted that the calculation diverges during the transverse vibration. The 2DOF movement of the responding cylinder will be studied with 3D model with RANS turbulence model in high Reynolds numbers conditions for the best approximation to engineering reality. To deal with the computationally expensive 3D models, the parallel computing technique will be employed. In addition, possible options for the applied numerical model is listed in Table 5.1.

In terms of analysis and discussion, the force coefficient will be examined, and the detailed mechanism of the interaction will be further investigated by flow visualisation. The vortex patterns and streak lines will be compared with flow regimes classified by Tatsuno & Bearman [108]. The occurrence of resonance at  $f_1 = 0.8f_n$  rather than  $f_1 = f_n$  will be further discussed with links to the added mass. Quantitative relationship between input parameters and the output data will be constructed.

Further researches may also investigate other computational fluid dynamics topics such as VIV energy harvesting and micro-organism flagella motion.

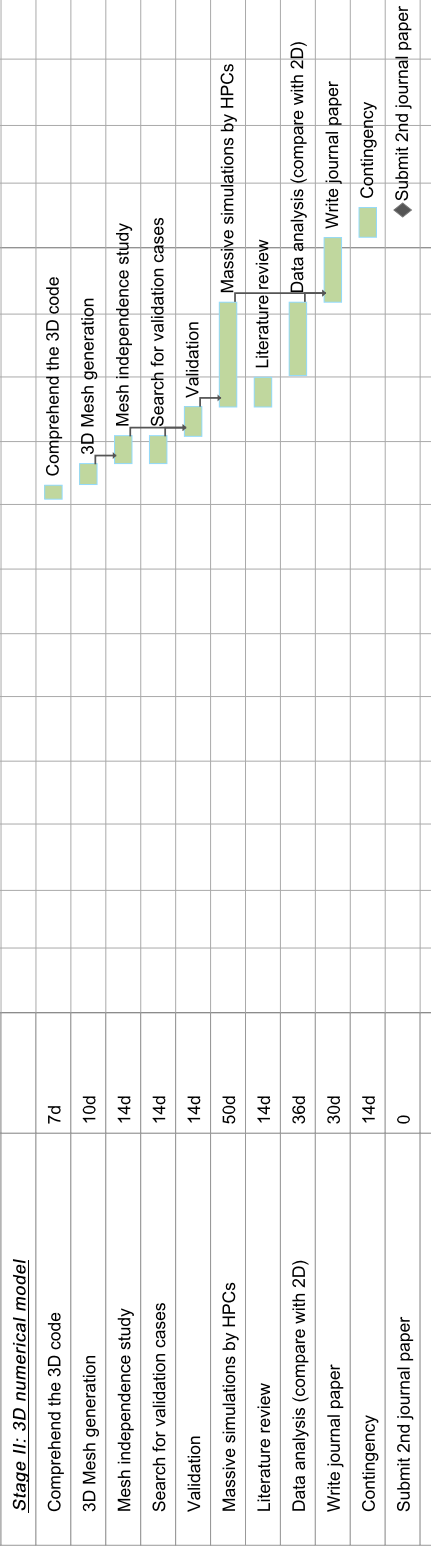
A research timetable in the form of Gantt chart is presented in the next two pages.

Table 5.1 Simulation Options

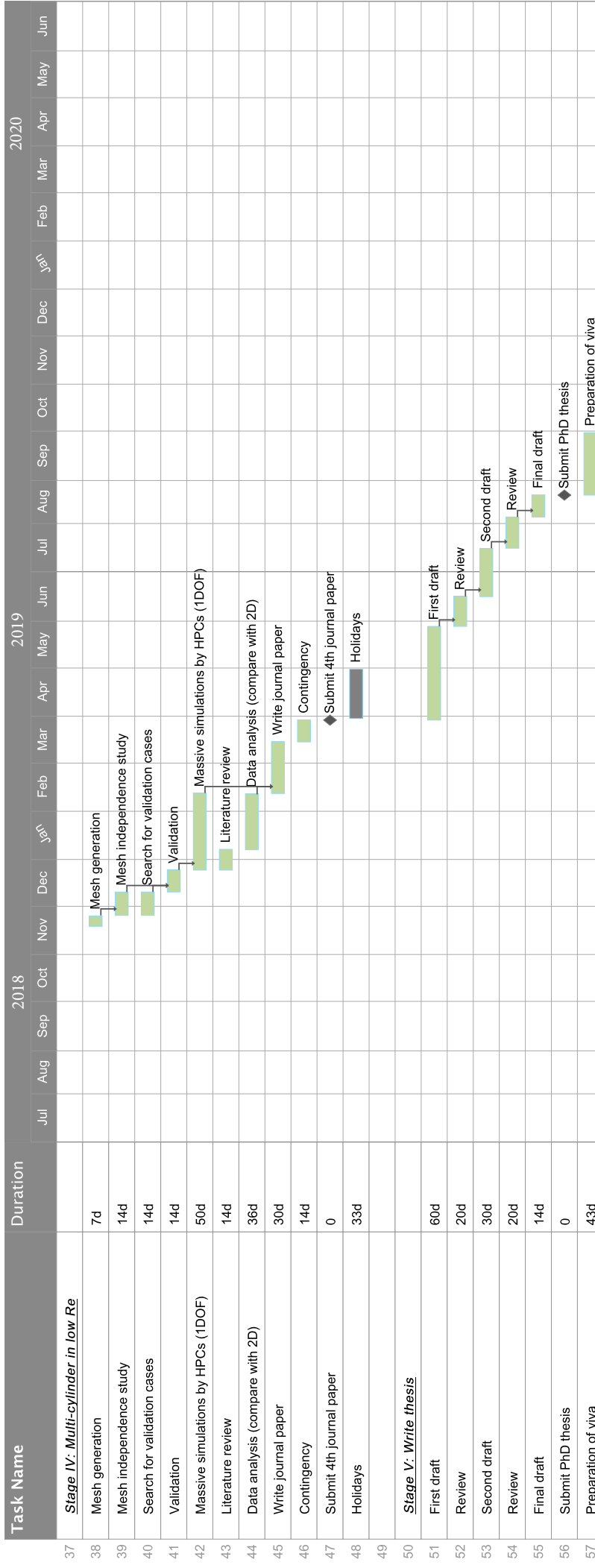
Dimensions	2D	3D
<b>DOF for Cylinder 2</b>	1DOF	2DOF
<b>Motion of Cylinder 1</b>	Inline	Transverse
<b>Turbulence Model</b>	DNS (low $Re_m$ )	RANS (high $Re_m$ )
<b>NS Equations</b>	Incompressible (water, low $m^*$ )	Compressible (air, high $m^*$ )

# Research Timetable Part 1

Task Name	Duration	Jul	Aug	Sep	Oct	Nov	Dec	Jan	Feb	Mar	Apr	May	Jun	Jul	Aug	Sep	Oct	Nov	Dec	Jan	Feb	Mar	Apr	May	Jun	
<b>2016</b>																										
1 <i>Stage I: 2D numerical model</i>																										
2 Comprehend the 2D code	9d																									
3 Investigate transverse vibration	14d																									
4 Preparation of ICHD	3d																									
5 ICHD conference	7d																									
6 Holidays	33d																									
7 Massive simulations by HPC	122d																									
8 Data analysis	81d																									
9 Writing journal paper	32d																									
10 Contingency	7d																									
11 Submit 1st journal paper	0																									
12																										
<b>2017</b>																										
13 <i>Stage II: 3D numerical model</i>																										
14 Comprehend the 3D code	7d																									
15 3D Mesh generation	10d																									
16 Mesh independence study	14d																									
17 Search for validation cases	14d																									
18 Validation	14d																									
19 Massive simulations by HPCs	50d																									
20 Literature review	14d																									
21 Data analysis (compare with 2D)	36d																									
22 Write journal paper	30d																									
23 Contingency	14d																									
24 Submit 2nd journal paper	0																									
25																										
26 <i>Stage III: 3D RANS model (high Re)</i>																										
27 Comprehend RANS model	7d																									
28 Mesh independence study	7d																									
29 Validation	7d																									
30 Massive simulations by HPCs	50d																									
31 Literature review	14d																									
32 Data analysis (compare with 2D)	36d																									
33 Write journal paper	30d																									
34 Contingency	21d																									
35 Submit 3rd journal paper	0																									



# Research Timetable Part 2



# References

- [1] MIT Towing Tank Lab. Advances in Vortex Induced Vibrations. URL <http://web.mit.edu/towtank/www/viv.html>.
- [2] Wikipedia. Vortex-induced vibration — Wikipedia, The Free Encyclopedia, 2015. URL [https://en.wikipedia.org/w/index.php?title=Vortex-induced\\_vibration&oldid=665042590](https://en.wikipedia.org/w/index.php?title=Vortex-induced_vibration&oldid=665042590).
- [3] USA-02139 Center for Ocean Engineering, MIT, Cambridge, MA. Vortex Induced Vibration Data Repository. URL <http://web.mit.edu/towtank/www/vivdr/datasets.html>.
- [4] VORTEX HYDRO ENERGY. URL <http://www.vortexhydroenergy.com/invention/>.
- [5] P Bearman. Vortex shedding from oscillating bluff bodies. *Annual Review of Fluid Mechanics*, 16(1):195–222, 1984. ISSN 0066-4189. doi: 10.1146/annurev.fluid.16.1.195.
- [6] Ming Zhao. Flow induced vibration of two rigidly coupled circular cylinders in tandem and side-by-side arrangements at a low Reynolds number of 150. *Physics of Fluids*, 25(12):123601, 2013. ISSN 10706631. doi: 10.1063/1.4832956. URL <http://scitation.aip.org/content/aip/journal/pof2/25/12/10.1063/1.4832956>.
- [7] Ming Zhao, Liang Cheng, and Tongming Zhou. Numerical simulation of vortex-induced vibration of a square cylinder at a low Reynolds number. *Physics of Fluids*, 25(2):023603, 2013. ISSN 10706631. doi: 10.1063/1.4792351. URL <http://scitation.aip.org/content/aip/journal/pof2/25/2/10.1063/1.4792351>.
- [8] C H K Williamson and R Govardhan. Vortex-Induced Vibrations. *Annual Review of Fluid Mechanics*, 36(1):413–455, 2004. ISSN 0066-4189. doi: 10.1146/annurev.fluid.36.050802.122128.
- [9] K. Vikestad, J. K. Vandiver, and C. M. Larsen. Added mass and Oscillation frequency for a circular cylinder subjected to vortex-induced vibration and external disturbance. *Journal of Fluids and Structures*, 14(14):1071–1088, oct 2000. ISSN 08899746. doi: 10.1006/jfls.2000.0308. URL <http://linkinghub.elsevier.com/retrieve/pii/S0889974600903086> <http://discovery.ucl.ac.uk/73002/>.
- [10] T. Sarpkaya. Vortex-induced oscillations: a selective review. *Journal of Applied Mechanics*, 46(2):241–258, 1979. ISSN 00218936. doi: 10.1115/1.3424537. URL <http://link.aip.org/link/?JAMCAV/46/241/1>.

- [11] C C Feng. The measurement of vortex induced effects in flow past stationary and oscillating circular and d-section cylinders. *Retrospective Theses and Dissertations, 1919-2007*, 1968.
- [12] A. Khalak and C.H.K. Williamson. Motions, Forces and Mode Transitions in Vortex-Induced Vibrations At Low Mass-Damping. *Journal of Fluids and Structures*, 13(7-8): 813–851, 1999. ISSN 0889-9746. doi: 10.1006/jfls.1999.0236.
- [13] D Brika and A Laneville. Vortex-induced vibrations of a long flexible circular cylinder. *Journal of Fluid Mechanics*, 250:481–508, 1993. ISSN 1469-7645. doi: 10.1017/S0022112093001533.
- [14] A Khalak and C H K Williamson. DYNAMICS OF A HYDROELASTIC CYLINDER WITH VERY LOW MASS AND DAMPING. *Journal of Fluids and Structures*, 10 (5):455–472, 1996. ISSN 0889-9746. doi: 10.1006/jfls.1996.0031.
- [15] Asif Khalak and Charles H.K. Williamson. Investigation of relative effects of mass and damping in vortex-induced vibration of a circular cylinder. *Journal of Wind Engineering and Industrial Aerodynamics*, 69-71:341–350, jul 1997. ISSN 01676105. doi: 10.1016/S0167-6105(97)00167-0. URL <http://linkinghub.elsevier.com/retrieve/pii/S0167610597001670>.
- [16] R Govardhan and C H K Williamson. Modes of vortex formation and frequency response of a freely vibrating cylinder. *Journal of Fluid Mechanics*, 420:85–130, 2000. ISSN 0022-1120. doi: 10.1017/s0022112000001233.
- [17] O M Griffin. Vortex-Excited Cross-Flow Vibrations of a Single Cylindrical Tube. *Journal of Pressure Vessel Technology*, 102(2):158–166, 1980. ISSN 0094-9930. URL <http://dx.doi.org/10.1115/1.3263315>.
- [18] R A Skop and S Balasubramanian. A new twist on an old model for vortex-excited vibrations. *Journal of Fluids and Structures*, 11(4):395–412, 1997.
- [19] P. Anagnostopoulos and P. W. Bearman. Response characteristics of a vortex-excited cylinder at low reynolds numbers. *Journal of Fluids and Structures*, 6(1):39–50, 1992. ISSN 10958622. doi: 10.1016/0889-9746(92)90054-7.
- [20] F. S. Hover, a. H. Techet, and M. S. Triantafyllou. Forces on oscillating uniform and tapered cylinders in cross flow. *Journal of Fluid Mechanics*, 363:97–114, 1998. ISSN 00221120. doi: 10.1017/S0022112098001074.
- [21] R. A. Skop and S. Balasubramanian. A new twist on an old model for vortex-excited vibrations. *Journal of Fluids and Structures*, 11(4):395–412, 1997. ISSN 08899746. doi: 10.1006/jfls.1997.0085. URL <http://www.scopus.com/inward/record.url?eid=2-s2.0-0000655294&partnerID=tZOTx3y1>.
- [22] A. Torum and N. M. Anand. Free Span Vibrations of Submarine Pipelines in Steady Flows—Effect of Free-Stream Turbulence on Mean Drag Coefficients. *Journal of Energy Resources Technology*, 107(4):415–420, 1985. ISSN 0195-0738. doi: 10.1115/1.3231212. URL <http://dx.doi.org/10.1115/1.3231212>.

- [23] John H. Lienhard. Synopsis of lift, drag, and vortex frequency data for rigid circular cylinders, 1966. URL <http://www.uh.edu/engines/vortexcylinders.pdf>.
- [24] E. Achenbach and E. Heinecke. On vortex shedding from smooth and rough cylinders in the range of Reynolds numbers  $6 \times 10^3$  to  $5 \times 10^6$ . *Journal of Fluid Mechanics*, 109(-1):239, apr 2006. ISSN 0022-1120. doi: 10.1017/S002211208100102X. URL [http://journals.cambridge.org/abstract\\_S002211208100102X](http://journals.cambridge.org/abstract_S002211208100102X).
- [25] Anatol Roshko. Some measurements of flow in a rectangular cutout. Technical report, DTIC Document, 1955.
- [26] A. H. Techet. 13.42 Lecture: Vortex Induced Vibrations. *Massachusetts Institute of Technology: MIT OpenCourseWare*, (April): 32, 2005. URL [http://ocw.mit.edu/courses/mechanical-engineering/2-22-design-principles-for-ocean-vehicles-13-42-spring-2005/readings/lec20\\_viv1.pdf](http://ocw.mit.edu/courses/mechanical-engineering/2-22-design-principles-for-ocean-vehicles-13-42-spring-2005/readings/lec20_viv1.pdf).
- [27] M. M. Zdravkovich. REVIEW—Review of Flow Interference Between Two Circular Cylinders in Various Arrangements. *Journal of Fluids Engineering*, 99(4):618, 1977. ISSN 00982202. doi: 10.1115/1.3448871.
- [28] M.M. Zdravkovich. The effects of interference between circular cylinders in cross flow. *Journal of Fluids and Structures*, 1(2):239–261, 1987. ISSN 08899746. doi: 10.1016/S0889-9746(87)90355-0.
- [29] D. Sumner. Two circular cylinders in cross-flow: A review. *Journal of Fluids and Structures*, 26(6):849–899, 2010. ISSN 08899746. doi: 10.1016/j.jfluidstructs.2010.07.001.
- [30] C. H. K. Williamson. Evolution of a single wake behind a pair of bluff bodies. *Journal of Fluid Mechanics*, 159(-1):1, 1985. ISSN 0022-1120. doi: 10.1017/S002211208500307X.
- [31] H J Kim. Investigation of the flow between a pair of circular cylinders in the flopping regime. *Journal of Fluid Mechanics*, 196(-1):431, 1988. ISSN 0022-1120. doi: 10.1017/s0022112088002769.
- [32] Md Mahbub Alam, M Moriya, and H Sakamoto. Aerodynamic characteristics of two side-by-side circular cylinders and application of wavelet analysis on the switching phenomenon. *Journal of Fluids and Structures*, 18(3):325–346, 2003.
- [33] Yuji Tasaka, Seiji Kon, Lionel Schouveiler, and Patrice Le Gal. Hysteretic mode exchange in the wake of two circular cylinders in tandem. *Physics of Fluids (1994-present)*, 18(8):84104, 2006.
- [34] Jiro Mizushima and Norihisa Suehiro. Instability and transition of flow past two tandem circular cylinders. *Physics of Fluids*, 17(10), 2005. ISSN 10706631. doi: 10.1063/1.2104689.

- [35] J.R. Meneghini, F. Saltara, C.L.R Siqueira, and J.A. Ferrari Jr. Numerical Simulataion of Flow Interference Between Two Circular Cylinders in Tandem and side-by-Side Arrangements. *Journal of Fluids and Structures*, 16(15):399–413, 2001. ISSN 08899746. doi: 10.1006/jfls.2001.0434. URL <http://www.sciencedirect.com/science/article/pii/S0889974600904341>.
- [36] D Brika and A Laneville. The flow interaction between a stationary cylinder and a downstream flexible cylinder. *Journal of Fluids and Structures*, 13(5):579–606, 1999. ISSN 08899746. doi: 10.1006/jfls.1999.0220.
- [37] E Fontaine, Jean-Pierre Morel, Yves-Marie Scolan, T Rippol, and Others. Riser interference and VIV amplification in tandem configuration. In *The Fifteenth International Offshore and Polar Engineering Conference*. International Society of Offshore and Polar Engineers, 2005.
- [38] F. J. Huera-Huarte and M. Gharib. Flow-induced vibrations of a side-by-side arrangement of two flexible circular cylinders. *Journal of Fluids and Structures*, 27(3):354–366, 2011. ISSN 08899746. doi: 10.1016/j.jfluidstructs.2011.01.001.
- [39] P Anagnostopoulos and G Iliadis. Numerical study of the flow pattern and the in-line response of a flexible cylinder in an oscillating stream. *Journal of Fluids and Structures*, 12(3):225–258, 1998.
- [40] S Mittal and V Kumar. Finite element study of vortex-induced cross-flow and in-line oscillations of a circular cylinder at low Reynolds numbers. *International Journal for Numerical Methods in Fluids*, 31(7):1087–1120, 1999. ISSN 02712091. doi: 10.1002/(SICI)1097-0363(19991215)31:7<1087::AID-FLD911>3.0.CO;2-C. URL [http://doi.wiley.com/10.1002/\(SICI\)1097-0363\(19991215\)31:7%3C1087::AID-FLD911%3E3.0.CO;2-C](http://doi.wiley.com/10.1002/(SICI)1097-0363(19991215)31:7%3C1087::AID-FLD911%3E3.0.CO;2-C).
- [41] S Mittal and V Kumar. Flow-Induced Oscillations of Two Cylinders in Tandem and Staggered Arrangements. *Journal of Fluids and Structures*, 15(5):717–736, 2001. ISSN 08899746. doi: 10.1006/jfls.2000.0376.
- [42] S. Mittal \* and V. Kumar. Vortex Induced Vibrations of a Pair of Cylinders at Reynolds Number 1000. *International Journal of Computational Fluid Dynamics*, 18(7):601–614, 2004. ISSN 1061-8562. doi: 10.1080/1061856031000137017.
- [43] W Jester and Y Kallinderis. Numerical study of incompressible flow about transversely oscillating cylinder pairs. *Journal of Offshore Mechanics and Arctic Engineering*, 126(4):310–317, 2004.
- [44] Subhankar Sen and Sanjay Mittal. Free vibration of a square cylinder at low Reynolds numbers. *Journal of Fluids and Structures*, 27(5-6):875–884, 2011. ISSN 08899746. doi: 10.1016/j.jfluidstructs.2011.03.006.
- [45] A. Joly, S. Etienne, and D. Pelletier. Galloping of square cylinders in cross-flow at low Reynolds numbers. *Journal of Fluids and Structures*, 28:232–243, 2012. ISSN 08899746. doi: 10.1016/j.jfluidstructs.2011.12.004.

- [46] Zhi Peng Zang and Fu Ping Gao. Steady current induced vibration of near-bed piggyback pipelines: Configuration effects on VIV suppression. *Applied Ocean Research*, 46:62–69, 2014. ISSN 01411187. doi: 10.1016/j.apor.2014.02.004.
- [47] Mehran Rahamanian, Liang Cheng, Ming Zhao, and Tongming Zhou. Vortex induced vibration and vortex shedding characteristics of two side-by-side circular cylinders of different diameters in close proximity in steady flow. *Journal of Fluids and Structures*, 48:260–279, 2014. ISSN 10958622. doi: 10.1016/j.jfluidstructs.2014.03.004.
- [48] MING Zhao and Liang CHENG. Two-dimensional numerical study of vortex shedding regimes of oscillatory flow past two circular cylinders in side-by-side and tandem arrangements at low Reynolds numbers. *Journal of fluid mechanics*, 751:1–37, 2014. ISSN 0022-1120. doi: 10.1017/jfm.2014.268. URL <http://cat.inist.fr/?aModele=afficheN&cpsidt=28605663>.
- [49] Ming Zhao, Joshua M Murphy, and Kenny Kwok. Numerical simulation of vortex-induced vibration of two rigidly connected cylinders in side-by-side and tandem arrangements using RANS model. *Journal of Fluids Engineering*, 138(2):21102, 2016.
- [50] K. Lam and S. C. Lo. A visualization study of cross-flow around four cylinders in a square configuration. *Journal of Fluids and Structures*, 6(1):109–131, 1992. ISSN 10958622. doi: 10.1016/0889-9746(92)90058-B.
- [51] Ming Zhao, Liang Cheng, Hongwei An, and Feifei Tong. Flow and flow-induced vibration of a square array of cylinders in steady currents. *Fluid Dynamics Research*, 47(4):45505, 2015.
- [52] K. Lam, J. Y. Li, K. T. Chan, and R. M C So. Flow pattern and velocity field distribution of cross-flow around four cylinders in a square configuration at a low Reynolds number. *Journal of Fluids and Structures*, 17(5):665–679, 2003. ISSN 08899746. doi: 10.1016/S0889-9746(03)00005-7.
- [53] A. T. Sayers. Flow interference between four equispaced cylinders when subjected to a cross flow. *Journal of Wind Engineering and Industrial Aerodynamics*, 31(1):9–28, 1988. ISSN 01676105. doi: 10.1016/0167-6105(88)90185-7.
- [54] A. T. Sayers. Vortex shedding from groups of three and four equispaced cylinders situated in a cross flow. *Journal of Wind Engineering and Industrial Aerodynamics*, 34(2):213–221, 1990. ISSN 01676105. doi: 10.1016/0167-6105(90)90145-3.
- [55] K Lam and X Fang. The effect of interference of four equispaced cylinders in cross flow on pressure and force coefficients. *Journal of Fluids and Structures*, 9(2):195–214, 1995.
- [56] K Lam, J Y Li, and R M C So. Force coefficients and Strouhal numbers of four cylinders in cross flow. *Journal of Fluids and Structures*, 18(3):305–324, 2003.
- [57] K. Lam and L. Zou. Three-dimensional numerical simulations of cross-flow around four cylinders in an in-line square configuration. *Journal of Fluids and Structures*, 26(3):482–502, 2010. ISSN 08899746. doi: 10.1016/j.jfluidstructs.2010.01.001.

- [58] K. Lam and L. Zou. Experimental study and large eddy simulation for the turbulent flow around four cylinders in an in-line square configuration. *International Journal of Heat and Fluid Flow*, 30(2):276–285, 2009. ISSN 0142727X. doi: 10.1016/j.ijheatfluidflow.2009.01.005.
- [59] T Farrant, M Tan, and W G Price. A cell boundary element method applied to laminar vortex-shedding from arrays of cylinders in various arrangements. *Journal of Fluids and Structures*, 14(3):375–402, 2000. ISSN 08899746. doi: 10.1006/jfls.1999.0275. URL <http://dx.doi.org/10.1006/jfls.1999.0275>.
- [60] Zhaolong Han, Dai Zhou, Xiaolan Gui, and Jiahuang Tu. Numerical study of flow past four square-arranged cylinders using spectral element method. *Computers & Fluids*, 84:100–112, 2013. ISSN 00457930. doi: 10.1016/j.compfluid.2013.05.008.
- [61] Feifei Tong, Liang Cheng, Ming Zhao, Tongming Zhou, and Xiao Bo Chen. The vortex shedding around four circular cylinders in an in-line square configuration. *Physics of Fluids*, 26(2), 2014. ISSN 10897666. doi: 10.1063/1.4866593.
- [62] A Nicolle and I Eames. Numerical study of flow through and around a circular array of cylinders. *Journal of Fluid Mechanics*, 679:1–31, 2011. ISSN 0022-1120. doi: Doi10.1017/Jfm.2011.77.
- [63] Ming Zhao, Liang Cheng, Hongwei An, and Feifei Tong. Flow and flow-induced vibration of a square array of cylinders in steady currents. *Fluid Dynamics Research*, 47(4):045505, aug 2015. ISSN 0169-5983. doi: 10.1088/0169-5983/47/4/045505. URL <http://stacks.iop.org/1873-7005/47/i=4/a=045505?key=crossref.b9b0a1a051ed33357f780eb4e15eeefd>.
- [64] Ling-Hui Yu, Jie-min Zhan, and Yok-sheung Li. Numerical investigation of drag force on flow through circular array of cylinders. *Journal of Hydrodynamics*, 25(3):330–338, 2013. ISSN 10016058. doi: 10.1016/S1001-6058(11)60371-6. URL <http://linkinghub.elsevier.com/retrieve/pii/S1001605811603716>.
- [65] C. Sweeney and C. Meskell. Fast numerical simulation of vortex shedding in tube arrays using a discrete vortex method. *Journal of Fluids and Structures*, 18(5):501–512, 2003. ISSN 08899746. doi: 10.1016/j.jfluidstructs.2003.08.009.
- [66] N. K.-R. Kevlahan and J. Wadsley. Suppression of three-dimensional flow instabilities in tube bundles. *Journal of Fluids and Structures*, 20(4):611–620, 2005. ISSN 08899746. doi: 10.1016/j.jfluidstructs.2005.02.010. URL <http://www.sciencedirect.com/science/article/pii/S0889974605000447>.
- [67] S J Price, M P Paidoussis, and B Mark. Flow Visualization of the Interstitial Cross-Flow through Parallel Triangular and Rotated Square Arrays of Cylinders. *Journal of Sound and Vibration*, 181(1):85–98, 1995. ISSN 0022460X. doi: 10.1006/jsvi.1995.0127.
- [68] N. K R Kevlahan. The role of vortex wake dynamics in the flow-induced vibration of tube arrays. *Journal of Fluids and Structures*, 27(5-6):829–837, 2011. ISSN 08899746. doi: 10.1016/j.jfluidstructs.2011.03.023.

- [69] M P Paiudoussis and S J Price. The mechanisms underlying flow-induced instabilities of cylinder arrays in crossflow. *Journal of Fluid Mechanics*, 187:45–59, 1988.
- [70] About FEM, 2016. URL <https://intranet.birmingham.ac.uk/collaboration/hpc-research/fem/about/index.aspx>.
- [71] Galerkin method, 2016. URL [https://en.wikipedia.org/wiki/Galerkin\\_method](https://en.wikipedia.org/wiki/Galerkin_method).
- [72] Finite element method, 2016. URL [https://en.wikipedia.org/wiki/Finite\\_element\\_method](https://en.wikipedia.org/wiki/Finite_element_method).
- [73] O.C. Zienkiewicz, R.L. Taylor, and J.Z. Zhu. The Finite Element Method: its Basis and Fundamentals. In *The Finite Element Method: its Basis and Fundamentals*, pages 573–640. 2013. ISBN 9781856176330. doi: 10.1016/B978-1-85617-633-0.00017-4. URL <http://www.sciencedirect.com/science/article/pii/B9781856176330000174>.
- [74] R. W. Clough. The finite element method in plane stress analysis. In *Proceedings of the 2nd Conference on Electronic Computation of American Society of Civil Engineers*, pages 345–378, 1960.
- [75] Olivier De Weck and Yong Il. Finite element method MIT lecture note. Technical report, 2004. URL [http://web.mit.edu/16.810/www/16.810\\_L4\\_CAE.pdf](http://web.mit.edu/16.810/www/16.810_L4_CAE.pdf).
- [76] Yunan Prawoto. *Integration of mechanics into materials science research: A guide for material researchers in analytical, computational and experimental methods*. Lulu. com, 2013.
- [77] Junuthula Narasimha Reddy. *An introduction to the finite element method*, volume 2. McGraw-Hill New York, 1993.
- [78] O C Zienkiewicz, R L Taylor, and P Nithiarasu. The Finite Element Method for Fluid Dynamics. *The Finite Element Method for Fluid Dynamics (Seventh Edition)*, 2014. doi: <http://dx.doi.org/10.1016/B978-1-85617-635-4.00001-7>. URL <http://www.sciencedirect.com/science/article/pii/B9781856176354000017>.
- [79] Jean Donea, S Giuliani, and Jean-Pierre Halleux. An arbitrary Lagrangian-Eulerian finite element method for transient dynamic fluid-structure interactions. *Computer methods in applied mechanics and engineering*, 33(1-3):689–723, 1982.
- [80] Arbitrary Lagrangian-Eulerian method. URL [http://www.me.sc.edu/research/jzuo/Contents/ALE/ALE\\_1.htm](http://www.me.sc.edu/research/jzuo/Contents/ALE/ALE_1.htm).
- [81] Transition and Turbulence. URL [https://www.princeton.edu/\\$\sim\\$asmits/Bicycle\\_web/transition.html](https://www.princeton.edu/$\sim$asmits/Bicycle_web/transition.html).
- [82] Yang Zhiyin. Large-eddy simulation: Past, present and the future. *Chinese Journal of Aeronautics*, 28(1):11–24, 2015. ISSN 10009361. doi: 10.1016/j.cja.2014.12.007.
- [83] Parviz Moin and Krishnan Mahesh. DIRECT NUMERICAL SIMULATION: A Tool in Turbulence Research. *Annu. Rev. Fluid Mech.*, 30:539–78, 1998.
- [84] Marten. Landahl and E. Mollo-Christensen. *Turbulence and random processes in fluid mechanics*. Cambridge University Press, 2nd edition, 1992. ISBN 9780521422130.

- [85] Gilles Eggenspieler and Senior. Turbulence Modelling, 2012. URL [http://fluid.itcmp.pwr.wroc.pl/\\$sim\\$plasiak/CFD/UsefulInformation/turbulence-summary-4.pdf](http://fluid.itcmp.pwr.wroc.pl/$sim$plasiak/CFD/UsefulInformation/turbulence-summary-4.pdf).
- [86] Kaustav Sengupta, Farzad Mashayek, and Gustaaf Jacobs. Direct numerical simulation of turbulent flows using spectral method. *46th AIAA Aerospace Sciences Meeting and Exhibit*, 2008. doi: 10.2514/6.2008-1450.
- [87] Gary N Coleman and Richard D Sandberg. A Primer on direct numerical simulation of turbulence – methods, procedures and guidelines, 2010. URL [http://eprints.soton.ac.uk/66182/1/A\\_primer\\_on\\_DNS.pdf](http://eprints.soton.ac.uk/66182/1/A_primer_on_DNS.pdf).
- [88] Large eddy simulation (wikipedia), 2015. URL [https://en.wikipedia.org/wiki/Large\\_eddy\\_simulation](https://en.wikipedia.org/wiki/Large_eddy_simulation).
- [89] Carl Barcock. RR Virtual Engine, 2014. URL <https://connect.innovateuk.org/documents/3329929/12298392/The+Virtual+Engine+-+Carl+Barcock,Rolls-Royce.pdf/3a87ffa6-3e9a-4f79-b137-9584516f7fb9>.
- [90] Reynolds-averaged Navier–Stokes equations, 2015. URL [https://en.wikipedia.org/wiki/Reynolds-averaged\\_Navier%25E2%2580%2593Stokes\\_equations#cite\\_note-1](https://en.wikipedia.org/wiki/Reynolds-averaged_Navier%25E2%2580%2593Stokes_equations#cite_note-1).
- [91] Robert D. Moser and Parviz Moin. The effects of curvature in wall-bounded turbulent flows. *Journal of Fluid Mechanics*, 175(-1):479, feb 1987. ISSN 0022-1120. doi: 10.1017/S0022112087000491. URL [http://www.journals.cambridge.org/abstract\\_S0022112087000491](http://www.journals.cambridge.org/abstract_S0022112087000491).
- [92] Low-pass filter (en.wikipedia.org). URL [https://en.wikipedia.org/wiki/Low-pass\\_filter](https://en.wikipedia.org/wiki/Low-pass_filter).
- [93] Elias Balaras and Ugo Piomelli. Wall-layer models for large-eddy simulations. *Annual Review of Fluid Mechanics*, 34, 2002.
- [94] Philippe R. Spalart. Detached-Eddy Simulation. *Annual Review of Fluid Mechanics*, 41(1):181–202, jan 2009. ISSN 0066-4189. doi: 10.1146/annurev.fluid.010908.165130. URL <http://www.annualreviews.org/doi/10.1146/annurev.fluid.010908.165130>.
- [95] Heinz Pitsch. LARGE-EDDY SIMULATION OF TURBULENT COMBUSTION. *Annual Review of Fluid Mechanics*, 38(1):453–482, jan 2006. ISSN 0066-4189. doi: 10.1146/annurev.fluid.38.050304.092133. URL <http://www.annualreviews.org/doi/10.1146/annurev.fluid.38.050304.092133>.
- [96] Rodney O. Fox. Large-Eddy-Simulation Tools for Multiphase Flows. *Annual Review of Fluid Mechanics*, 44(1):47–76, jan 2012. ISSN 0066-4189. doi: 10.1146/annurev-fluid-120710-101118. URL <http://www.annualreviews.org/doi/10.1146/annurev-fluid-120710-101118>.
- [97] J. Smagorinsky. General circulation experiments wiht the primitive equations I. The basic experiment. *Monthly Weather Review*, 91(3):99–164, 1963. ISSN 0036-8075. doi: 10.1126/science.27.693.594.

- [98] K-omega models – CFD-Wiki, the free CFD reference, 2016. URL [http://www.cfd-online.com/Wiki/K-omega\\_models](http://www.cfd-online.com/Wiki/K-omega_models).
- [99] K-omega turbulence model, 2016. URL [https://en.wikipedia.org/wiki/K%25E2%2580%2593omega\\_turbulence\\_model#CITEREFWilcox2008](https://en.wikipedia.org/wiki/K%25E2%2580%2593omega_turbulence_model#CITEREFWilcox2008).
- [100] SST k-omega model – CFD-Wiki, the free CFD reference, jul 2016. URL [http://www.cfd-online.com/Wiki/SST\\_k-omega\\_model](http://www.cfd-online.com/Wiki/SST_k-omega_model).
- [101] SST k-omega governing equations, 2013. URL <http://help.autodesk.com/cloudhelp/2014/ITA/SimCFD/files/GUID-0F5C4828-9F91-46B6-A16A-2578D72DCFCC.htm>.
- [102] Wikibooks. Fluid Mechanics/Dimensional Analysis — Wikibooks, The Free Textbook Project, 2015. URL [https://en.wikibooks.org/w/index.php?title=Fluid\\_Mechanics/Dimensional\\_Analysis&oldid=3013142](https://en.wikibooks.org/w/index.php?title=Fluid_Mechanics/Dimensional_Analysis&oldid=3013142).
- [103] H. DÜTSCH, F. DURST, S. BECKER, and H. LIENHART. Low-Reynolds-number flow around an oscillating circular cylinder at low Keulegan–Carpenter numbers. *Journal of Fluid Mechanics*, 360:249–271, apr 1998. ISSN 00221120. doi: 10.1017/S002211209800860X. URL [http://journals.cambridge.org/abstract\\_S002211209800860X](http://journals.cambridge.org/abstract_S002211209800860X).
- [104] Zhendong Cui, Ming Zhao, and Bin Teng. Vortex-induced vibration of two elastically coupled cylinders in side-by-side arrangement. *Journal of Fluids and Structures*, 44: 270–291, jan 2014. ISSN 0889-9746. doi: 10.1016/j.jfluidstructs.2013.11.007.
- [105] MING Zhao and Liang Cheng. Two-dimensional numerical study of vortex shedding regimes of oscillatory flow past two circular cylinders in side-by-side and tandem arrangements at low Reynolds numbers. *Journal of fluid mechanics*, 751:1–37, 2014. ISSN 0022-1120. doi: 10.1017/jfm.2014.268. URL <http://cat.inist.fr/?aModele=afficheN&cpsidt=28605663>.
- [106] Ming Zhao, Liang Cheng, and Tongming Zhou. Numerical simulation of vortex-induced vibration of a square cylinder at a low Reynolds number. *Physics of Fluids*, 25(2), 2013. ISSN 10706631. doi: 10.1063/1.4792351.
- [107] Alexandra Techet. 2.016 Hydrodynamics. *Massachusetts Institute of Technology: MIT OpenCourseWare*, pages 1–9, 2005. URL <http://ocw.mit.edu>.
- [108] M Tatsuno and P W Bearman. A visual study of the flow around an oscillating circular cylinder at low Keulegan–Carpenter numbers and low Stokes numbers. *Journal of Fluid Mechanics*, 211:157–182, 1990.

